The Parametrically Forced Pendulum

Broer, H.W.; Hoveijn, I.; Noort, M. van; Simó, C.; Vegter, G.

Published in:
Journal of dynamics and differential equations

Publication date:
2004

Journal of Dynamics and Differential Equations, Vol. 16, No. 4, October 2004 (© 2004)

The Parametrically Forced Pendulum: A Case Study in $1\frac{1}{2}$ Degree of Freedom*

H.W. Broer, I. Hoveijn, M. van Noort[1], C. Simó and G. Vegter

Received October 31, 2002

This paper is concerned with the global coherent (i.e., non-chaotic) dynamics of the parametrically forced pendulum. The system is studied in a $1\frac{1}{2}$ degree of freedom Hamiltonian setting with two parameters, where a spatio-temporal symmetry is taken into account. Our explorations are restricted to large regions of coherent dynamics in phase space and parameter plane. At any given parameter point we restrict to a bounded subset of phase space, using KAM theory to exclude an infinitely large region with rather trivial dynamics. In the absence of forcing the system is integrable. Analytical and numerical methods are used to study the dynamics in a parameter region away from integrability, where the analytic results of a perturbation analysis of the nearly integrable case are used as a starting point. We organize the dynamics by dividing the parameter plane in fundamental domains, guided by the linearized system at the upper and lower equilibria. Away from integrability some features of the nearly integrable coherent dynamics persist, while new bifurcations arise. On the other hand, the chaotic region increases.

KEY WORDS: Hamiltonian dynamics; Bifurcations; Numerical methods; KAM theory.

2000 Mathematical Subject Classification: 37J20, 37J40, 37M20, 70H08.

1. INTRODUCTION

We consider a parametrically forced pendulum in a Hamiltonian $1\frac{1}{2}$ degree of freedom setting, given by the equation of motion

$$\ddot{x} = (\alpha + \beta \cos t) \sin x. \tag{1}$$

Here $x \in \mathbb{S}^1$ is the deviation from the upper equilibrium and ranges over the whole circle. The equation is given in 'inverted pendulum format',

* Dedicated to Professor Shui-Nee Chow on the occasion of his 60th birthday.

[1] E-mail: m.vannoort@imperial.ac.uk

1040-7294/04/1000-0897/0

meaning that $x=0$ corresponds to the upper equilibrium, where the pendulum stands up, while $x=\pi$ denotes the lower equilibrium, where it hangs down. The independent variable is $t\in\mathbb{S}^1$. The parameters $\alpha,\beta\in\mathbb{R}$ correspond to the square of the eigenfrequency of the (free) pendulum at the lower equilibrium, and the amplitude of the forcing, respectively. Indeed, $\alpha=\sqrt{g/\ell}$, where g denotes the gravitational acceleration and ℓ the length of the pendulum. Without loss of generality we restrict to $\alpha,\beta\geqslant 0$.

This system is widely studied within the context of classical perturbation theory, that is, locally in several regions in phase and parameter space. Most notably, there is a long history of research of the Mathieu equation. This is the linearized equation of the forced pendulum at its equilibria, and it governs the stability of these points. See Fig. 1 for a stability diagram, also compare Mathieu [57], van der Pol and Strutt [71], Stoker [79], Meixner and Schäfke [65], Hale [39,40], Weinstein and Keller [83,84], Levi *et al.* [50,56], and Broer *et al.* [18,24,25].

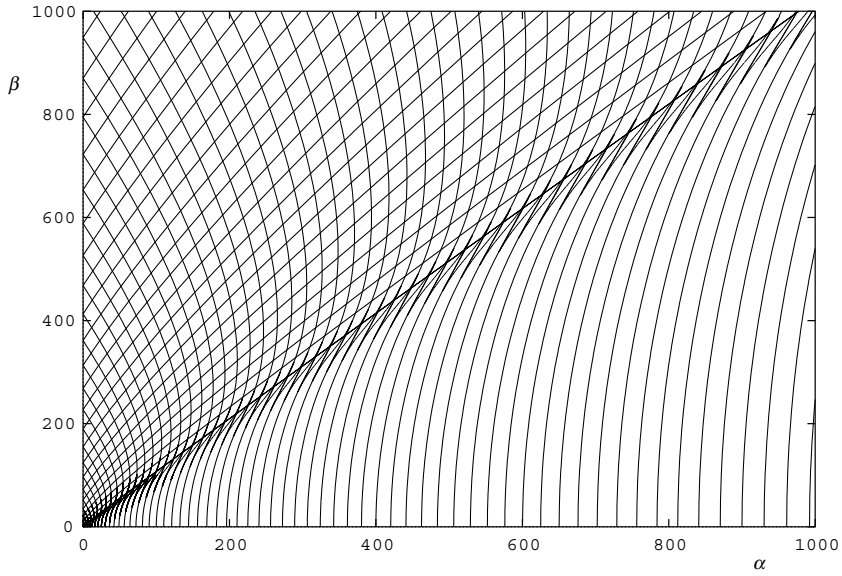

Figure 1. Numerically computed stability diagram of the parametrically forced pendulum (1) on a large scale, revealing a checkerboard structure. On the curves going from the left towards the top side the stability of the upper equilibrium changes, on the curves coming from the α axis the lower equilibrium changes stability. Except near the diagonal $\alpha=\beta$, every line consists, in fact, of two stability curves, that are extremely close together. Hence the stable regions of the upper equilibrium are extremely narrow, as are those of the lower equilibrium above the diagonal, while below this diagonal the unstable regions of the lower equilibrium are very small, compare [19].

The non-linear system is nearly integrable for small β/α. This permits a local bifurcation analysis at the two equilibria, near the resonance points of the lower equilibrium on the α axis, see Broer and Vegter [28], and near the degenerate point $(\alpha, \beta) = (0, 0)$, see Broer *et al.* [12, 13].

The existence of invariant tori can be shown using KAM theory, see Kolmogorov [47], Arnol'd [4], and Moser [60]. Again the nearly integrable case of small β/α is a natural perturbative setting, but other settings are possible, e.g., see Moser [63, 64], Chierchia and Zehnder [30], and You [85], also compare Levi [51–53] for a discussion of a similar system.

1.1. Setting of the Problem and Sketch of the Results

In contrast with the approaches sketched above, the present paper has a more global perspective, as it aims to explore the coherent (i.e., non-chaotic) dynamics of the forced pendulum, in dependence of the parameters (α, β) in the whole phase space and parameter plane. By coherent dynamics we mean all non-chaotic phenomena, that is, all periodic and quasi-periodic dynamics, and their bifurcations. Emphasis lies on orbits of low period, since these usually generate the largest stability islands, cf. [51].

This study combines perturbation theory and numerical tools, adopting the programme of Broer *et al.* [26]. Indeed, analytical results obtained in certain parameter regions serve as a framework and a starting point for numerical continuation to a larger part of parameter space. Furthermore, at representative parameter points phase portraits are computed. Such an interaction between analytical and numerical methods has proven to be a fruitful approach in the study of systems of this complexity.

We obtain the following two main results. Firstly, at any parameter point (α, β) there exists a bounded 'region of interest' such that outside this region the dynamics consists of a set of invariant tori of large measure, with thin layers of resonant dynamics in between. Secondly, the parameter plane can be divided in boxes, so-called 'fundamental domains'. Theoretical and numerical evidence is presented that this structure organizes an important part of the coherent dynamics.

Let us discuss these results in more detail. Our explorations mostly deal with the Poincaré map P of the forced pendulum, defined on the cylindrical section $t = 0 \mod 2\pi\mathbb{Z}$. This map has a spatial and a temporal symmetry, see Fig. 2 for some example phase portraits. Fig. 3 explains the coding of periodic points and bifurcations that will be used throughout this paper.

For any parameter point (α, β), the coherent dynamics of P at sufficiently large $|y|$ consists of invariant circles (of rotational type, i.e.,

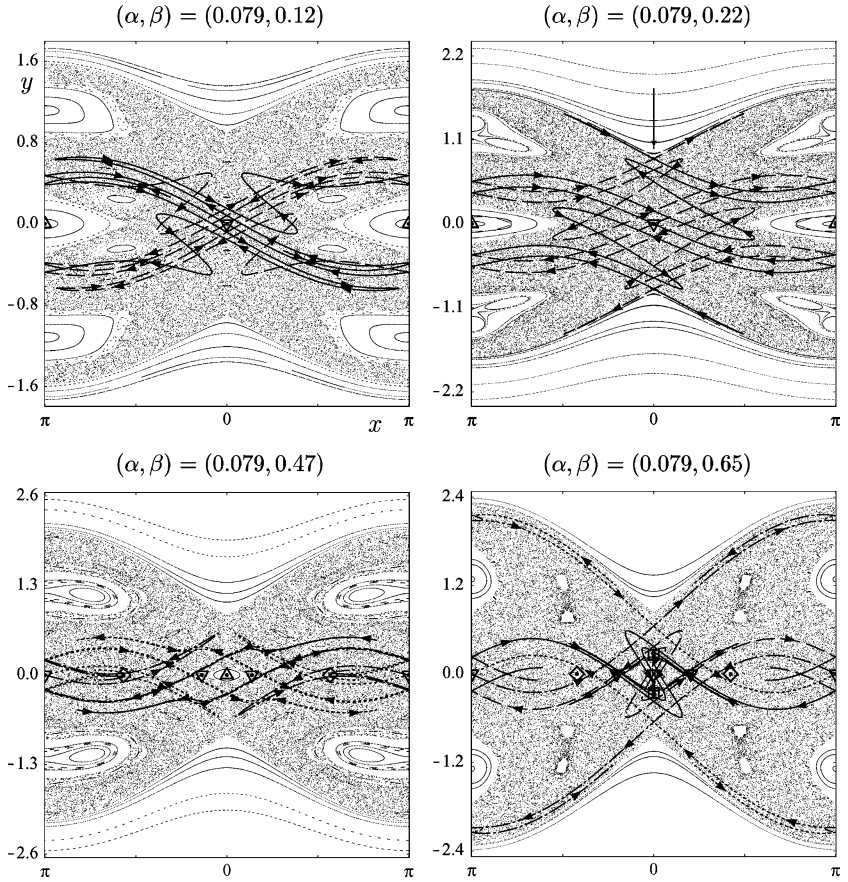

Figure 2. Phase portraits of the Poincaré map at $\alpha = 0.079$, for various β, as indicated. Outside a 'region of interest', the dynamics mainly consists of invariant circles winding around the cylinder. Inside, the region of chaos increases with β, but coherent dynamics remains present. Both equilibria undergo period doubling and pitchfork bifurcations. Parts of invariant manifolds of (unstable) equilibria are also plotted. Invariant manifolds and periodic points born at the equilibria are marked according to the coding in Fig. 3. In some diagrams there are unmarked stable fixed points above and below the lower equilibrium, corresponding to resonant orbits of the vector field X with frequency 1 in the x-direction. In the bottom left diagram, these fixed points have destabilized in a period doubling bifurcation. For more details, we refer to Section 1.1.

winding around the cylindrical phase space) with confined chaotic motion and strings of islands in between. We prove by KAM theory that the measure of the set of invariant circles is exponentially close to full measure as $|y| \to \infty$. This region of invariant circles and small islands therefore is excluded from the analysis, thereby restricting to a 'region of interest' in

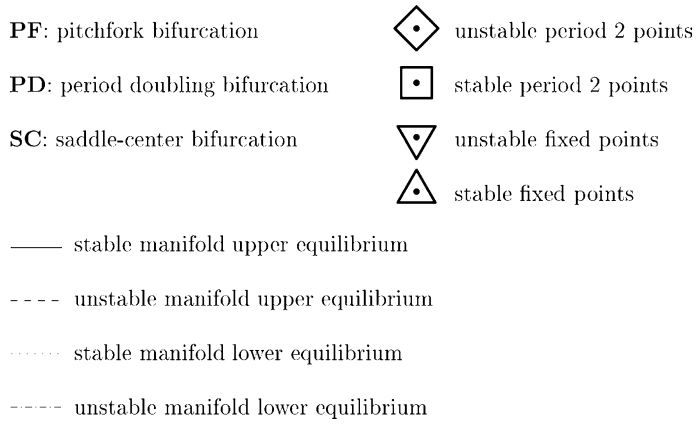

Figure 3. Coding of periodic points, invariant manifolds of equilibria, and bifurcations of the Poincaré map, used in phase portraits, bifurcation and stability diagrams.

phase space. We note that for the free pendulum this coincides with the region between the separatrices. A very accurate numerical estimate on a large domain in the parameter plane, supported by asymptotic theoretical estimates, shows that the 'region of interest' is bounded by $y \approx \pm 2\sqrt{\alpha \pm \beta}$ for all sufficiently large $(\alpha, \beta) \in \mathbb{R}^2_{\geqslant 0}$. For a rigorous bound, using KAM theory, we refer to [21].

In the 'region of interest', we organize our explorations by dividing the parameter plane into so-called fundamental domains, based on the stability types of the upper and lower equilibria. Fig. 4 shows the corresponding stability diagrams in the (α, β) plane, where shading indicates stability. The stability boundaries are curves of pitchfork (PF) or period doubling (PD) bifurcations, as indicated, where the pitchfork bifurcation has codimension one due to a spatial symmetry of the system, that will be explained below.

Combining the two stability diagrams we see that the parameter plane consists of regions of four different types, depending on the stability types of the two equilibria. These regions are collected mostly in groups of four, one of each type, forming what will be called *fundamental domains*, again see Fig. 4, also compare Fig. 5 for a sketch of one domain. The boundaries of these domains are formed by stability curves. Most fundamental domains belong to four types, depending on the bifurcation type of their boundaries. Indeed, these domains have four sides, where opposite sides correspond to different bifurcation types, either PF or PD, leading to a total of four possibilities.

The fundamental domains mostly appear in blocks of 2×2 domains, one of each type, again see Fig. 5. Moving across such a block, both

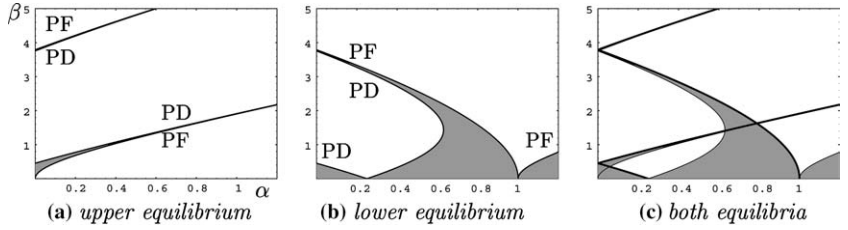

Figure 4. Part of the (numerically computed) stability diagrams of the equilibria of the pendulum (1), first separate, then combined. Shading indicates stability. The diagrams are symmetric around the α axis. At curves labeled 'PF' or 'PD' pitchfork bifurcations or period doubling bifurcations take place, respectively. In the rightmost diagram, thickened curves correspond to boundaries of fundamental domains.

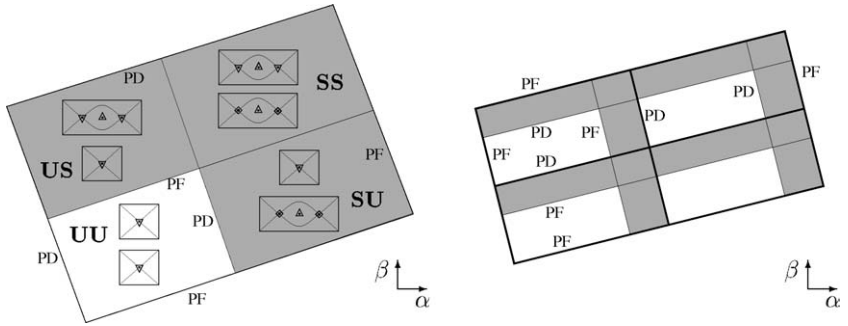

Figure 5. Left: Sketch of one fundamental domain, with an indication of the stability types and bifurcations of the two equilibria. The bifurcations on the stability boundaries depend on the type of fundamental domain. In each region the upper equilibrium is in the top phase portrait, and the lower in the bottom one. Right: Sketch of one block of 2×2 fundamental domains (bounded by thick lines), where the bifurcation types of the stability boundaries are indicated.

'horizontally' and 'vertically', one intersects two stability boundaries of PF type (where the trace of the linearized Poincaré map at the relevant equilibrium equals 2), two of PD type (where the trace is -2), and finally another one of PF type, in that order.

Part of the coherent dynamics of the nonlinear system is governed by the fundamental domains. Indeed, for small β/α, normal form theory yields an integrable approximation to P, valid near the two equilibria, cf. [12,13,28]. This is continued numerically to larger parameter values. The approximation shows that the stability types and bifurcations of the upper and lower equilibria (and hence the appearance of stable regions) are the same in fundamental domains of the same type. We note that below the diagonal $\alpha=\beta$ there is a single row of fundamental domains. The lower

equilibrium is mostly stable here, and hence this region contains the largest part of the coherent, near integrable dynamics of the full problem.

Away from integrability we find other local bifurcations that involve large stable domains in phase space. These are also investigated by numerical means, and it turns out that their codimension one bifurcation curves follow the fundamental domain structure in the parameter plane. This leads us to the conjecture that the fundamental domains organize a substantial part of the global coherent dynamics.

Remarks:

1. A Fig. 2 illustrates, the islands between the rotational invariant circles (outside the 'region of interest') are very hard to detect, since the largest ones are close to the chaotic domain. As an example, we have plotted a period 4 island in the top right diagram passing through $(x, y) = (0.0915)$ (indicated by the arrow). This island intersects the line $x = 0$ between $y = 0.914$ and $y = 0.926$, and goes horizontally from -0.14 to 0.14, where the related hyperbolic period 4 points are located.
2. For most (α, β) the 'region of interest' also includes orbits that in the integrable case $\beta = 0$ lie outside this region. For example, the large stable domains above and below the lower equilibrium in the phase portraits of Fig. 2 lie inside the 'region of interest', but correspond to a resonant invariant circle with rotation number one in the integrable system.

1.2. Acknowledgments

We thank Boele Braaksma, Alan Champneys, Francesco Fassò, Àngel Jorba, Bernd Krauskopf, and Evgeny Verbitski for valuable discussion during the preparation of this paper. The research of the fourth author has been partially supported by grants BFM2003-09504-C02-01 (Spain), 2001SGR-70 (Catalonia) and INTAS00-221. The computer clusters (HIDRA and EIXAM) of the UB-UPC Dynamical Systems Group have been widely used.

1.3. Overview

Let us give a short overview of the contents of this paper. In Section 2 the system is introduced and some properties regarding symmetries and linearization are discussed. Section 3 applies KAM theory to show persistence of Diophantine invariant circles of P, and gives estimates on the measure of the union of these circles and on the size of the 'region

of interest'. Adiabatic estimates on this size are given in Appendix A. In Section 4 the Poincaré map P is studied in several fundamental domains.

2. PRELIMINARIES

In this section some properties of the system, like symmetries, are discussed. The system (1) of the parametrically forced pendulum can be written as a vector field

$$X(x, y, t; \alpha, \beta) = \frac{\partial}{\partial t} + y\frac{\partial}{\partial x} - (\alpha + \beta\rho(t))V'(x)\frac{\partial}{\partial y}, \tag{2}$$

where $y = \dot{x}$ denotes velocity as before, $(x, y, t) \in \mathbb{S}^1 \times \mathbb{R} \times \mathbb{S}^1$, $\rho(t) = \cos t$, $V(x) = \cos x - 1$, and $(\alpha, \beta) \in \mathbb{R}^2$. This vector field is Hamiltonian, with time-dependent Hamilton function

$$H(x, y, t; \alpha, \beta) = \frac{1}{2}y^2 + (\alpha + \beta\rho(t))V(x). \tag{3}$$

The vector field X has several symmetries. Since V is even, it has a spatial symmetry given by $\mathcal{S}: (x, y, t) \mapsto (-x, -y, t)$. This means that $\mathcal{S}_* X = X$, and X is called $\mathcal{S}$-equivariant. Furthermore, X is $\mathcal{R}$-reversible, meaning that $\mathcal{R}_* X = -X$, where the temporal symmetry $\mathcal{R}: (x, y, t) \mapsto (-x, -y, t)$ is due to the evenness of ρ. There are other symmetries, involving both phase and parameter space. Indeed, since $V(x) = -V(x + \pi)$, X is $\mathcal{T}$-equivariant, where $\mathcal{T}: (x, y, t; \alpha, \beta) \mapsto (x + \pi, y, t; -\alpha, -\beta)$. Finally, X is $\mathcal{U}$-equivariant, with $\mathcal{U}: (x, y, t; \alpha, \beta) \mapsto (x, y, t + \pi; \alpha, -\beta)$, because $\rho(t) = -\rho(t + \pi)$. By these two symmetries without loss of generality we can restrict to the first quadrant $\alpha, \beta \geqslant 0$ of the parameter plane.

Since the system is 2π-periodic in time, it is natural to consider its Poincaré or stroboscopic map P on the section $t = 0$, corresponding to the flow over time 2π of X. The map P is defined implicitly by

$$(P(x, y), 2\pi) = X^{2\pi}(x, y, 0),$$

where X^t is the flow over time t of X. Since X is divergence free, P is area and orientation preserving. Moreover it inherits the symmetries of X. This means that P is S-equivariant and R-reversible, that is, $SPS = P$ and $RPR = P^{-1}$, where $S: (x, y) \mapsto (-x, -y)$ and $R: (x, y) \mapsto (x, -y)$. The symmetries $\mathcal{T}$ and $\mathcal{U}$ also carry over to symmetries of P in a trivial way.

The stability of the two equilibria is determined by the linearized system, given by the so-called Mathieu equation

$$\ddot{x} = (\alpha + \beta\rho(t))x.$$

The Poincaré map of the Mathieu equation equals the linearization of the map P at the upper equilibrium. Thus the Mathieu equation at the parameter point (α, β) determines the stability of the upper equilibrium $(x, y, t) = (0, 0, t)$ at (α, β), and, by the symmetry $\mathcal{T}$ of the nonlinear system, the stability of the lower equilibrium $(x, y, t) = (\pi, 0, t)$, at $(-\alpha, -\beta)$. Hence, combining the stability diagram of the Mathieu equation with a copy rotated around the origin over angle π results in a diagram where each parameter point shows the stability type of both equilibria, resulting in the checkerboard of fundamental domains shown in Figs. 1 and 4. (Because of the symmetry $\mathcal{U}$ the copy can also be reflected in the β-axis instead of rotated.)

We introduce a codification of the checkerboard. Each fundamental domain can be identified by a pair (column number, row number), starting with (1,1), as illustrated in Fig. 6. The stability regions in a fundamental domain can be identified by a third label equal to one of the strings 'UU', 'US', 'SU', 'SS', where the former (latter) letter determines the stability of the lower (upper) equilibrium; 'U' means unstable and 'S' stable.

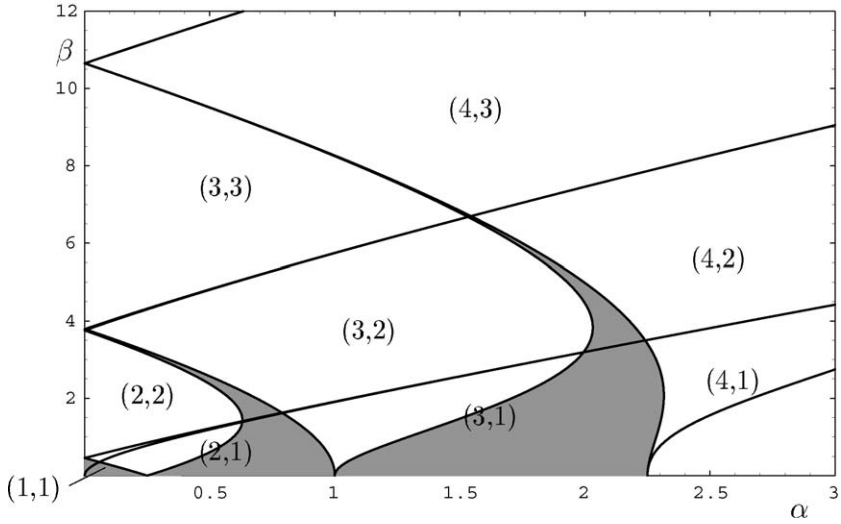

Figure 6. The stability diagram of the parametrically forced pendulum is a checkerboard of fundamental domains, that mostly consist of four stability regions. The domains are bounded by thickened (black) curves and codified as indicated. In the shaded regions the lower or upper equilibrium is stable. (In many domains these regions are too narrow to be seen).

Remark.

In [12,13,28] more general cases of V and ρ are considered, where the symmetries $\mathcal{S}$ and $\mathcal{R}$ are optional, while $\mathcal{T}$ and $\mathcal{U}$ play no role. In the present paper we restrict to the simplest case with maximal symmetry, and take the potential function $V(x)=\cos x-1$ of the pendulum and the forcing function $\rho(t)=\cos t$ of the classical Mathieu case.

3. INVARIANT CIRCLES AND THE 'REGION OF INTEREST'

It is well known from KAM theory that for y sufficiently large and satisfying a Diophantine condition, the dynamics of P is almost completely quasi-periodic, compare Moser [63,64], Chierchia and Zehnder [30], and You [85]. In between these invariant circles of quasi-periodic motion one generically expects confined chaotic motion and strings of islands, also called Poincaré-Birkhoff chains. Indeed, the Poincaré-Birkhoff theorem [16, 17] implies that in between any two invariant circles there exist periodic points of all intermediate rational rotation numbers.

In this section we obtain the following results. At any given parameter point (α,β), invariant circles of P with Diophantine rotation number exist for $y>C(\alpha,\beta)$, forming a Whitney smooth Cantor foliation of phase space. Here $C>0$ is some increasing function. Moreover, in our real-analytic setting the relative measure of invariant circles is $1-O(e^{-By})$ as $y\to+\infty$, for some constant $B>0$, i.e., $y=+\infty$ is a Lebesgue density 'point' of the union of invariant circles for all parameter values, compare, e.g., Broer *et al.* [14] and Pöschel [70].

Thus the dynamics for y sufficiently large is well known, and we can restrict to a bounded 'region of interest' in phase space by excluding the region of invariant circles and strings of islands. A bound on the 'region of interest' can be obtained by estimating the location of the 'lowest' invariant circle of P, that is, an invariant circle that is a graph over x with $y>0$ (i.e., it winds around the cylindrical phase space), and is sufficiently close to the circle $y=0$.

For a rigorous estimate, based on quantitative KAM theory, we refer to [21]. In this paper we present a numerical estimate in the region $[0,1000]\times[0,1000]$ in the parameter plane, showing that the 'lowest' invariant circle passes approximately through the point $(x,y)=(\pi,2\sqrt{\alpha+\beta})$ in phase space. Thus the 'region of interest' is approximately bounded by $y=2\sqrt{\alpha+\beta}$. This result is supported by two estimates based on adiabatic theory, namely $y=2\sqrt{\alpha}$, to first approximation as $\beta\to0$, and $y=2\sqrt{\alpha+\beta}$, to first approximation as $\alpha>\beta\to\infty$.

In the next subsection a perturbative setting suitable for KAM theory is obtained. In Section 3.2 we show persistence of invariant circles qualitatively, and obtain the asymptotics of the relative measure, while Section 3.3 is concerned with the numerical estimate on the size of the 'region of interest'. More details can be found in [21].

3.1. A Well Defined Perturbation Problem

To obtain a persistence result for large y we first need a well defined perturbation problem. For large y (compared to α and β) the motion of the forced pendulum is a small perturbation of motion on tori $y=$constant, with frequency vector $(\dot{x}, \dot{t}) = (y, 1)$. This suggests the following translation, where ω is a localization parameter denoting the first frequency:

Lemma 1. *Let $X = y\frac{\partial}{\partial x} + (\alpha + \beta\cos t)\sin x\frac{\partial}{\partial y} + \frac{\partial}{\partial t}$ be the vector field of the forced pendulum (2). Consider the localization.*

$$(x, y, t) \mapsto (\tilde{x}, \tilde{y}, \tilde{t}) = (x, y - \omega, t).$$

Then the transformed vector field is Hamiltonian, and given by

$$X(x, y, t; \alpha, \beta, \omega) = (\omega + y)\frac{\partial}{\partial x} + (\alpha + \beta\cos t)\sin x\frac{\partial}{\partial y} + \frac{\partial}{\partial t},$$

where the tildes are dropped for simplicity.

In the sequel the dependence on α and β is suppressed for simplicity. We note that the transformed vector field is $\mathcal{S}$-equivariant and $\mathcal{R}$- reversible, if the transformation $\omega \mapsto -\omega$ is included in the definition of these symmetries.

In the localized setting, y is considered to be a small variable, as compared to ω. Hence, the vector field at large ω (i.e., large y in the original setting) can be seen as a small perturbation of the integrable vector field $\omega\frac{\partial}{\partial x} + \frac{\partial}{\partial t}$. This vector field has a family of invariant tori $y = 0$, parameterized by ω. In the perturbed setting many of these still give rise to quasi-periodic dynamics, and their asymptotical relative measure can be estimated for $\omega \to +\infty$. In order to optimize this estimate, we average the system such that the non-integrable part is exponentially small as $\omega \to +\infty$. Embedding the phase space $\mathbb{S}^1 \times \mathbb{R} \times \mathbb{S}^1$ in $\mathbb{C}^3$, we obtain the following theorem.

Theorem 2. *Let $D \subset \mathbb{C}^3$ be a bounded region containing the torus y=0. Then there exists a neighborhood $\tilde{D}$ of D, such that for ω sufficiently large*

there exists an analytic, symplectic, time-preserving map $\Psi = \Psi_\omega : D \to \tilde{D}$, *piecewise analytic in* ω, *with*

$$\Psi - Id = O(\omega^{-1}) \text{ on } D, \text{as } \omega \to +\infty,$$

and

$$\begin{aligned} \Psi_*^{-1} X(x, y, t; \omega) &= X_0(y, t; \omega) + X_1(x, y, t; \omega), \text{ where} \\ X_0(y; \omega) &= f(y; \omega)\frac{\partial}{\partial x} + \frac{\partial}{\partial t}, \text{ and} \\ X_1(x, y, t; \omega) &= O(e^{-B\omega}) \text{ as } \omega \to +\infty, \end{aligned}$$

for some constant $B > 0$, *and a function* f *satisfying* $f = \omega + O(1)$ *as* $\omega \to +\infty$.

The proof of theorem 2 consists of averaging with respect to x, using Neishtadt's theorem for the estimates, compare, e.g., [9,22,23,36,43,66]. For more details we refer to [21].

3.2. Persistence of Measure of Invariant Circles

The unperturbed system X_0 of Theorem 2 has invariant tori $y = 0$ for each ω, with frequency vector $(\dot{x}, \dot{t}) = (f(0; \omega), 1)$. For sufficiently large ω, the function f is strictly increasing in ω, and hence can be regarded as a new parameter, that we again denote by ω. For more details on this construction we refer to [15,42, Section 5a]. Thus we obtain the system

$$X(x, y, t; \omega) = X_0(\omega) + X_1(x, y, t; \omega), \tag{4}$$

with

$$X_0(\omega) = \omega\frac{\partial}{\partial x} + \frac{\partial}{\partial t}, \text{ and } X_1 = O(e^{-B\omega}).$$

We now prove that the invariant torus $y = 0$ of X_0 with Diophantine frequency vector $(\omega, 1)$ persist under the perturbation X_1 if it is sufficiently small. Let the parameter ω range over an interval $\Omega = [\omega_m, \omega_M]$, with $\omega_M > \omega_m > 0$, and let

$$D = \{(x, y, t; \omega)\} = \mathbb{S}^1 \times \{0\} \times \mathbb{S}^1 \times \Omega$$

be a region in phase-parameter space that contains the invariant torus $y = 0$ of the unperturbed system. In this region the frequency ratio $\dot{x}/\dot{t}$ varies with ω, and in this sense the system is non-degenerate.

For $\sigma, \eta > 0$, let $D_{\sigma,\eta}$ be a complex neighborhood of D, given by

$$D_{\sigma,\eta} = (\mathbb{S}^1 + \eta) \times B(0, \sigma) \times (\mathbb{S}^1 + \eta) \times (\Omega + \sigma),$$

where $B(0,\sigma)$ is the closed ball in $\mathbb{C}$ with center 0 and radius σ, and for any, set $S\subset\mathbb{C}^n$ and any $\eta>0$,

$$S+\eta=\bigcup_{w\in S}\{z\in\mathbb{C}^n:|z-w|<\eta\}.$$

Furthermore, define the set Ω^γ of Diophantine frequencies in Ω by

$$\Omega^\gamma=\{\omega\in\Omega:|p\omega+q|\geqslant\gamma|(p,q)|^{-\tau}\text{ for all }(p,q)\in\mathbb{Z}^2\backslash\{0\}\}. \tag{5}$$

Here $\gamma>0$ is a parameter and $\tau>1$ is a constant.

The KAM theorem for divergence free vector fields with codimension 1 invariant tori, cf. [15,61], asserts the following: for ω_m sufficiently large, all invariant 2-tori of X_0 in D with frequency ω in Ω^γ and not too near the boundary of Ω, correspond to invariant 2-tori of the perturbed system X with the same frequency ratio ω. The perturbed invariant tori lie in a neighborhood of D in $\{(x,y,t;\omega)\}=\mathbb{S}^1\times\mathbb{R}\times\mathbb{S}^1\times\Omega$. The tori of X and X_0 are equivalent by a Whitney-smooth time-preserving diffeomorphism Ψ, depending on the parameters, that approximately maps D into D. The diffeomorphism Ψ is the identity in the t component, see [15,42, Section 7f].

The largeness condition on ω_m can be made explicit as follows. By the above theorem, there exists a constant $\delta>0$, depending only on η (so in particular independent of γ,τ,σ, and Ω), such that all tori $y=0$ of the unperturbed system X_0 with frequency ω in Ω^γ persist under the perturbation X_1 if $0<\gamma\leqslant\sigma<1$, and

$$|X_1|_{\sigma,\eta}:=\sup_{D_{\sigma,\eta}}\|X_1\|<\gamma\delta, \tag{6}$$

see [14, Section 5.2]. Since $|X_1|_{\sigma,\eta}=O(e^{-B(\omega_m+\sigma)})$, this condition is obviously satisfied for $\gamma=\sigma=O(e^{-\tilde{B}\omega_m})$ for some $\tilde{B}\in(0,B)$, and $\omega_m>0$ sufficiently large.

It remains to derive the asymptotics of the relative measure of invariant tori of X as $\omega_m\to+\infty$. Under condition 6, the relative measure of frequencies in Ω corresponding to persistent tori satisfies

$$\mu_{\text{rel}}(\Omega):=\frac{\mu(\Omega^\gamma)}{\mu(\Omega)}=1-O\left(\frac{\gamma}{\omega_M-\omega_m}\right)\ as\ \frac{\gamma}{\omega_M-\omega_m}\to 0,$$

cf. [14, Section 5.2]. Taking $\gamma=O(e^{-\tilde{B}\omega_m})$, we obtain the following theorem.

Theorem 3. *Let X be the vector field of the forced pendulum in the form of equation (4), and let $\Omega = [\omega_m, \omega_M]$ be an interval of frequencies. Choose constants $\tau > 2$ and $\eta > 0$. For ω_m sufficiently large, take $\gamma = O(e^{-\tilde{B}\omega_m})$ such that condition (6) is satisfied, and let Ω^γ be the set of Diophantine frequencies in Ω, defined by (5). Then the relative measure of persistent tori in Ω, defined as above, satisfies*

$$\mu_{rel}(\Omega) = 1 - O\left(\frac{e^{-\tilde{B}\omega_m}}{\omega_M - \omega_m}\right) \text{ as } \omega_m \to +\infty, \text{ with } \omega_M > \omega_m.$$

This theorem roughly states that the torus with frequency vector $(+\infty, 1)$ is a Lebesgue density point of the set of persistent tori. For the original system (2) this means the following: for large ω, one has $y \approx \omega$, where y is the phase variable in the original setting. Thus the invariant torus $y = +\infty$ of the original system is a Lebesgue density point of the set of invariant tori, and the relative measure is $1 - O(e^{-By})$ as $y \to +\infty$, for some constant $B > 0$.

Remarks.

1. In the usual KAM setting, one obtains a conjugacy between the perturbed and unperturbed tori, under the condition that the frequency map is non-degenerate, compare, e.g., [5,6,47,48]. In our case, the tori, are just equivalent in general, due to the fact that only the frequency ratio is non-degenerate.
2. The persistence result can also be obtained for the return map P of X on the section $t = 0$. In the localized setting of equation (4), it is a perturbation of the return map P_0 of X_0, given by

   $$P_0 : (x, y) \mapsto (x + 2\pi\omega, y).$$

   This is a pure twist map, having invariant circles $y = 0$ with rotation number ω, corresponding to the invariant 2-tori $y = 0$ of X_0, and persistence of circles with Diophantine rotation number follows from the twist theorem, cf. [60]. The conjugacy between the invariant circles of P_0 and P is given by the same diffeomorphism Ψ, restricted to the section $t = 0$ where P is defined.
3. This perturbative setting fails when we try to find the 'lowest' invariant circle of P, since the y-coordinate is not approximately constant on invariant circles near the 'region of interest', compare, e.g., Fig. 19 below. We plan to deal with this problem in [21].

3.3. Numerical Estimates of the 'Region of Interest'

By adiabatic theory, one can obtain the estimate $y \approx 2\sqrt{\alpha+\beta}$ for the boundary of the region of interest, where α and β are large, see Appendix A. We now estimate this boundary numerically, by computing the location of the 'lowest' invariant circle of P on three evenly spaced grids in the parameter plane, namely in the regions $\{(\alpha, \beta)\} = [0, 10] \times [0, 10]$ with step 0.05 in both variables, $\{(\alpha, \beta)\} = [0, 100] \times [0, 100]$ with step 0.05 and $\{(\alpha, \beta)\} = [0, 1000] \times [0, 1000]$ with step 10. By location we mean the y-coordinate y_π of the invariant circle at $x = \pi$. This is a good estimate for the maximal y coordinate on this circle. Indeed, numerical experiments suggest that y_π is a local maximum on the invariant circle, except in a small neighborhood of $(\alpha, \beta) = (0, 0.22)$. Moreover, the only other reasonable candidate (regarding the numerical experiments of Section 4) for a global maximum is the y value y_0 at $x = 0$, and numerical results in a large region in the parameter plane show that $y_\pi > y_0$ except in a small domain near the origin, see Fig. 7. The lower boundary of this domain is given by $\alpha = \frac{1}{2}\beta^3 + O(\beta^4)$, as illustrated in the figure. This is confirmed by a normal form computation. For details we refer to [21]. Moreover, we find that $y_0 < 2$ for $(\alpha, \beta) \in [0, 1000] \times [0, 1000]$, while $y_\pi \approx 2\sqrt{\alpha+\beta}$, in good agreement with the adiabatic estimate.

For a description of the method of computation of the location of the lowest invariant circle we refer to [21], also compare [77]. The left diagram of Fig. 8 shows this location in the region $[0, 10] \times [0, 10]$ in the parameter plane.

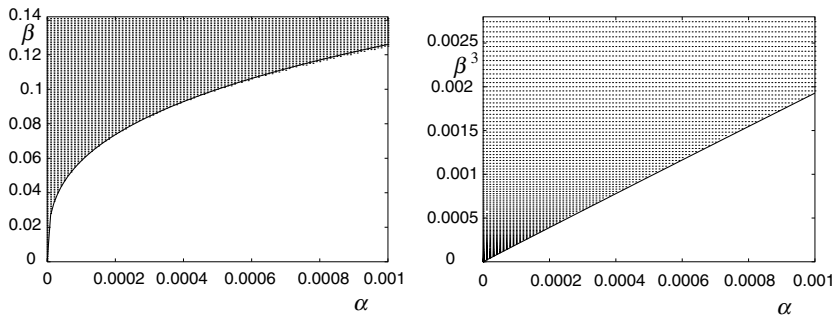

Figure 7. Left: region in the parameter plane where the y-coordinate y_0 of the 'lowest' invariant circle at $x = 0$ is larger than its y-coordinate y_π at $x = \pi$. The curve $\alpha = \frac{1}{2}\beta^3$, that approximates the lower boundary of the region, is also drawn. Right: the same region, in the (α, β^3)-plane, showing an even better approximation to the lower boundary, namely $\alpha = \frac{1}{2}\beta^3 - 0.15\beta^4$.

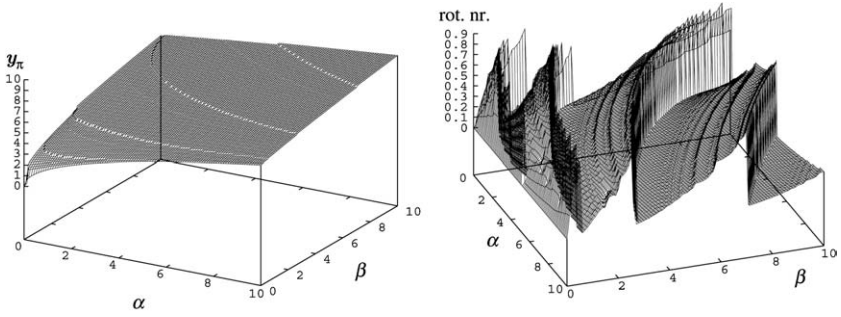

Figure 8. Left: graph over $(\alpha, \beta) \in [0, 10] \times [0, 10]$ of the location of the 'lowest' invariant circle of P, i.e., its intersection with $x = \pi$. Right: graph over the same domain of the rotation number of the same circle. The cliffs correspond to the jumps in the location of this circle.

In this diagram one clearly sees jumps in the location of the 'lowest' invariant circle. These are due to destruction of the 'lowest' invariant circle as β grows, resulting in a jump in the estimate to a higher invariant circle. This can be seen very well in the right diagram of the same figure, showing the rotation number of the 'lowest' invariant circle as a graph over (α, β). We observe steep cliffs where the rotation number jumps from a value near 1 to a value near 0, corresponding to jumps of the 'lowest' invariant circle over large stable domains.

Figure 9 shows the location of the 'lowest' invariant circle and the absolute difference ε_{abs} on the large grid $\{(\alpha, \beta)\} = [0, 1000] \times [0, 1000]$. Again we can see the location of the jumps. Moreover, it is clear that the absolute difference decreases as α and β increase. Table I presents for the three grids the maximal absolute and relative differences ε_{abs} and ε_{rel} between the numerical and adiabatic estimates. By relative difference we mean the absolute difference divided by the maximum of y_π and y_{adiab}.

Table I. The maximal relative difference ε_{rel} between the numerical and adiabatic estimates of the location of the 'lowest' invariant circle, in all three grids

grid	ε_{abs}	ε_{rel}	$\varepsilon_{\text{rel}}(5)$	$\varepsilon_{\text{rel}}(50)$	$\varepsilon_{\text{rel}}(500)$
10×10	0.77	0.92	0.11	–	–
100×100	0.67	0.32	0.10	0.021	–
1000×1000	0.35	0.049	0.049	0.014	0.0026

Further, $\varepsilon_{\text{rel}}(k)$ is the same difference restricted to the region $\|(\alpha, \beta)\| > k$ of the grid.

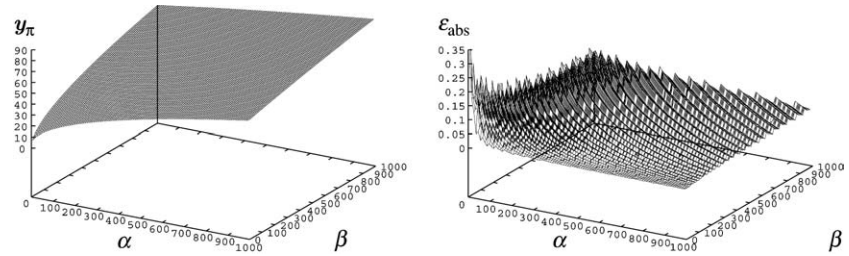

Figure 9. Left: graph over $(\alpha, \beta) \in [0, 1000] \times [0, 1000]$ of the location y_π of the 'lowest' invariant circle of P. Right: the absolute difference $\varepsilon_{\text{abs}} = |y_\pi - y_{\text{adiab}}|$ between the numerical and adiabatic estimates in the same domain.

In formula:

$$\varepsilon_{\text{rel}} = \left| \frac{y_\pi - y_{\text{adiab}}}{\max(|y_\pi|, |y_{\text{adiab}}|)} \right|.$$

The Table I also states, for several k, the maximal relative difference $\varepsilon_{\text{rel}}(k)$ in the part of the grid where $\|(\alpha, \beta)\| > k$. We conclude that the relative difference decreases rapidly when α and β increase.

To further verify our numerical results, we note that the adiabatic estimate y_{adiab} is constant on lines of constant $\alpha + \beta$. For the region $[0, 100] \times [0, 100]$ in the parameter plane, Fig. 10 shows the maximal and minimal values $y_{\max}$ and $y_{\min}$ of the numerical estimate in grid points on lines $\alpha + \beta =$constant, plotted against $\alpha + \beta$. In formula:

$$y_{\max}(\lambda) = \max_{\alpha,\beta}(y_\pi(\alpha, \beta)),$$

where the maximum is taken over all (α, β) in the grid with $\alpha + \beta = \lambda$, and $y_{\min}$ is defined analogously. As $\alpha + \beta$ increases the two graphs seem to converge, which again suggests that for large α, β the adiabatic estimate y_{adiab} is very accurate.

4. NUMERICAL STUDY OF THE COHERENT DYNAMICS

The goal of this section is to study the coherent (and to a lesser extent the non-coherent) dynamics of the Poincaré map in several fundamental domains in the parameter plane, and to determine to what extent this dynamics differs from one domain to another. In some fundamental domains near the origin of the parameter plane and some further away, this dynamics is described using both analytical and numerical means. An integrable approximation to the Poincaré map P, valid for small β, is used as a starting point for the investigation of the dynamics. Analytical

results regarding periodic orbits, their stability type and bifurcations can be extended to a larger part of the parameter plane by numerical continuation. Numerical methods (like continuation) also serve to describe aspects of the coherent dynamics not covered by the integrable model.

4.1. Method and Sketch of the Results

Let us now describe our method of research and its results in more detail. To describe the dynamics of P in an arbitrary fundamental domain, we start with an integrable approximation. This yields a 'skeleton' for the dynamics in any fundamental domain in the parameter plane, that is, it describes the stability types and bifurcations of the upper and lower equilibrium of the forced pendulum.

Using these analytical ingredients, the dynamics of the Poincaré map is investigated numerically. First, to get an overview of the phenomena that can occur, we simply compute phase portraits of the Poincaré map by numerical integration, where the locations of periodic points bifurcated from the equilibria and stable and unstable invariant manifolds of the equilibria (when unstable) are shown. Then follows an analysis of the observed dynamical objects. Here numerical continuation is used to obtain bifurcation diagrams, locate periodic points, and compute curves of codimension one bifurcation points in the parameter plane.

We consider some fundamental domains near the origin of the parameter plane, and only one farther away, since for large parameter

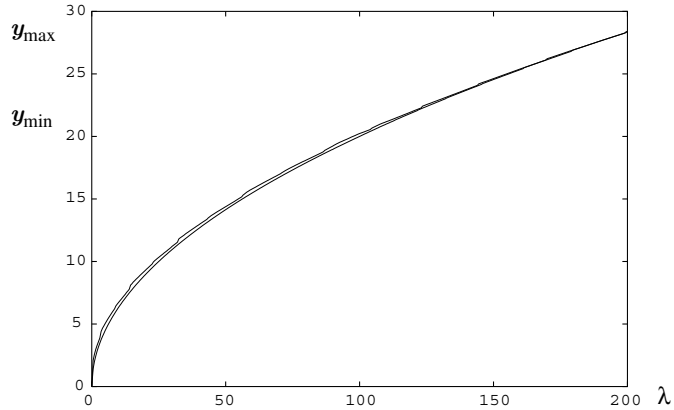

Figure 10. Graph over $\lambda \in [0, 200]$ of the maximal and minimal values of the location of the 'lowest' invariant circle in grid points on the line $\lambda = \alpha + \beta$.

values the Poincaré map restricted to the 'region of interest' is mainly chaotic, and seems to vary little (in a qualitative sense) with the parameters. The two equilibria are unstable except in very narrow regions in the parameter plane. Thus we conclude that, for fundamental domains far away from $(\alpha, \beta) = (0, 0)$ the Poincaré map has little coherent dynamics and is qualitatively the same in domains of the same type.

In the domains near the origin the coherent dynamics is very rich. To start with, we retrieve the bifurcations of the upper and lower equilibria that were found in the integrable skeleton. Because of the symmetries S and R the location of a periodic point born in a bifurcation at one of the equilibria is restricted to the lines $y = 0, x = 0$ and π.

There are several phenomena in these phase portraits that are not found in the skeleton. Numerically computed bifurcation diagrams show that the periodic points bifurcating from the upper and lower equilibrium rapidly undergo further bifurcations if they are stable. For numerical evidence that this is the start of period doubling cascades we refer to Kim and Hu [45] and McLaughlin [58]. All periodic points seem either to go towards the upper or lower equilibrium or to escape from the equilibria in the y direction as the parameter β increases.

Furthermore, there are large stable regions above and below the lower equilibrium, coming from the broken invariant circle winding around phase space with rotation number 1, i.e., consisting of points where the underlying vector field has frequency 1 in the x-direction. The fixed point in the center of the stable region undergoes period doubling and pitchfork bifurcations. Moreover, we find 1:3 resonance bifurcations here, and expect also $p:q$ resonances of higher order. Apparently the eigenvalues of the linearized Poincaré map at the fixed point move along the complex unit circle from the saddle-center position (where both eigenvalues are 1) at $\beta = 0$ to the period doubling position (where the eigenvalues are -1) at some nonzero β, passing through all resonance $e^{\pm 2\pi i p/q}$ in between.

There are more stable regions on the x-axis, originating from a saddle-center bifurcation. Both the stable and unstable period two points born at this bifurcation undergo pitchfork bifurcations.

At any periodic point subharmonic bifurcations occur when the eigenvalues of the linearized Poincaré map pass through a resonance. We investigate this for the two equilibria, concentrating on the 1:3 resonance. All bifurcations mentioned above take place on curves in the parameter plane, that for large parameter values either converge to the α axis or to one of the stability boundaries of the upper equilibrium.

Finally there is chaos. Invariant circles around stable periodic points (and those winding around phase space) are interlaced with resonant dynamics. Indeed, the Poincaré-Birkhoff theorem [16, 17] implies that in

between any two invariant circles there exist periodic points of all intermediate rational rotation numbers. Moreover, there is a 'chaotic sea' in the 'region of interest', that seems to grow as β increases. At the same time the stable domains in this region seem to get smaller, although their relative measure remains positive, due to the fact that the number of islands increases with α and β, see Neishtadt *et al.* [68] and Giorgilli *et al.* [38]. In particular this shows that there is no ergodicity in the whole region of interest, even at high parameter values.

The 'chaotic sea' mentioned above can be associated with a transversal hyperbolic periodic point that generates it by homoclinic intersections, as follows. When invariant manifolds of hyperbolic points have transversal intersections, most nearby orbits form clouds. It is generally conjectured that the closure of these orbits is an ergodic set of positive Lebesgue measure, see Arnol'd and Avez [1]. On the other hand, generically the 'chaotic sea' is densely filled with islands of elliptic periodic points, see Robinson [72]. So the 'chaotic sea' probably is a nowhere dense set of positive area. A similar phenomenon was first observed in the Hénon-Heiles system, cf. Hénon and Héiles [41] and, e.g., Moser [62], and can be found in many other examples.

Let us present an overview of the remainder of this section. The integrable skeleton is described in Section 4.2, the phase portraits of P are computed in Section 4.3, and Section 4.4 analyzes their dynamical features. Section 4.5 presents an extended stability diagram in the parameter plane, including curves of codimension one bifurcation points.

4.2. Integrable Skeleton

The nearly integrable Poincaré map for small β/α can be studied as perturbation problem, near any given point $(\alpha, \beta) = (\alpha_0, 0)$ on the α-axis, with β and the 'detuning' $\delta = \alpha - \alpha_0$ serving as perturbation parameters.

In [28] normal forms for the integrable approximating map are given at the resonance points of the lower equilibrium $(\alpha, \beta) = (\frac{1}{4}k^2, 0), k = 1, 2, \ldots$. Their local phase portraits at the lower equilibrium are reproduced in Fig. 11, compare [28, Fig. 8]. Up to a conjugacy the map P is an infinitely flat perturbation of the integrable approximation as the parameters go to the resonance point on the α axis and (x, y) tend to the lower equilibrium. Similar phase portraits for the degenerate point $(\alpha, \beta) = (0, 0)$ of the upper equilibrium are given in [12, Figs. 2,6] and [13, Figs. 2,4], and reproduced in Fig. 12. In this case the difference between P and the integrable approximation is infinitely flat as $(y, \alpha, \beta) \to (0, 0, 0)$, for all $x \in \mathbb{S}^1$.

One can show that all bifurcations (except subharmonics of period $\geqslant 3$) of the two equilibria are given by these integrable approximations,

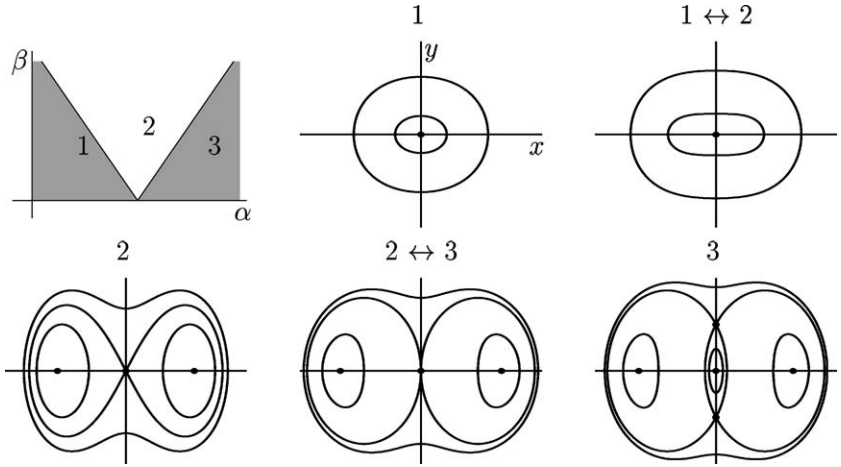

Figure 11. Stability diagram and phase portraits of an integrable approximation to P at a resonance point $(\alpha, \beta) = (\frac{1}{4}k^2, 0), k \in \mathbb{Z}_{>0}$, of the lower equilibrium. The stability boundaries have *k-th* order of contact at the resonance point (the case $k = 1$ is displayed). The bifurcations on the boundaries are of pitchfork type if k is even, and of period doubling type otherwise, and thus generate fixed and period two points, respectively. Apart from this, in our case of spatio-temporal symmetry, the phase portraits of the integrable approximation are qualitatively the same for all k.

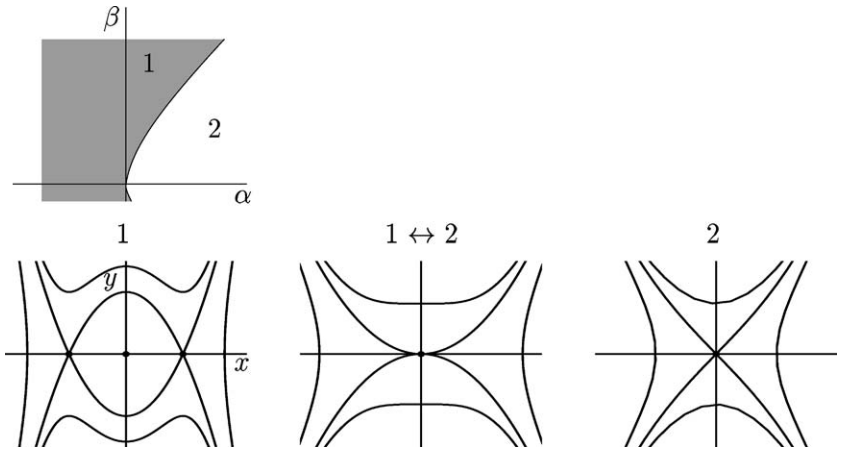

Figure 12. Stability diagram and phase portraits of an integrable approximation to P at the degenerate point $(\alpha, \beta) = (0, 0)$ of the upper equilibrium. The stability boundary consists of pitchfork bifurcations.

and hence the stability types and bifurcations of the equilibria (and the configuration of periodic points resulting from the bifurcations) are known at any parameter point. Figure 5 shows phase portraits of the skeleton in a single fundamental domain (of one of the four types, for the other types the bifurcations differ). Only those periodic points are shown that are involved in bifurcations at the equilibria taking place in this domain. We note that the schemes are not in proportion, and stability types of the periodic points bifurcating from the equilibria can change due to further bifurcations. Figure 13 displays the integrable skeleton for three domains near the origin of the parameter plane, showing all the periodic points bifurcated from the equilibria.

Remark. The lowest stability boundary of the upper equilibrium is a curve passing through $(\alpha, \beta) = (0, 0)$. The others are obtained by computing a stability boundary of the lower equilibrium and reflecting it in the βaxis. Thus the bifurcations of the upper equilibrium can easily be deduced from those of the lower equilibrium. Because of the symmetry involved here, the local phase portraits at the upper equilibrium have to be rotated over 90° compared to those of the lower equilibrium in Fig. 11, see Broer and Vegter [28].

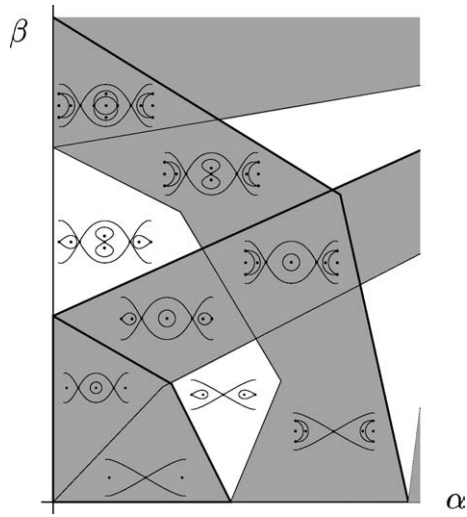

Figure 13. Sketch of the phase portraits of the integrable skeleton in three fundamental domains near the origin, where all periodic points bifurcated from the equilibria are indicated, as well as the direction (x or y) in which they bifurcate. The boundaries of the fundamental domains are indicated by thicker curves.

4.3. Phase Portraits

To get an overview of the dynamics of P we study its phase portraits at representative parameter points in the three fundamental domains $(1,1)$, $(2,1)$, and (2,2) near the origin of the parameter plane, and the domain $(12,6)$ farther away.

For the first three domains, representative parameter points are selected by computing phase portraits at lattice points in the parameter plane, and sorting out interesting ones. Since the regions in the domain has its own lattice, instead of a single lattice for the entire domain or the entire parameter plane. In domain (12,6), the stable regions are extremely tiny, and therefore phase portraits are computed at a few randomly chosen parameter points, in the region where both equilibria are unstable. Since there is a big difference between the first three domains and the last one, we treat them separately.

4.3.1. The Fundamental Domains Near the Origin of the Parameter Plane

The phase portraits in the fundamental domains (1,1), (2,1) and (2,2) are displayed in Figs. 14–18. Each figure shows a stability diagram and some phase portraits. The stability diagram displays the stability curves in the fundamental domain under consideration, drawn in black, while stability curves outside this domain are grayed. As before, regions (in the current fundamental domain) where the upper or lower equilibrium is stable are shaded. The stability diagram further displays, in each stability region, the phase portrait of the integrable skeleton.

The phase portraits show a representative collection of orbits of P, obtained simply by iteration using an integrator based on Taylor series expansion, cf. Broer and Simó [24], Simó [76, Appendix] or Jorba and Zou [44] for a discussion of this method. The integrator is very efficient and preserves the symmetries of the system.

Each diagram (except for the blowups) contains about 46,000 points; its caption states the parameter point (α, β) where the phase portrait is taken, and a diagram number corresponding to that in the stability diagram. In case the upper or lower equilibrium is unstable, (finite parts of) its invariant manifolds, computed by DsTool [10,46], are displayed. The locations and stability types of the upper and lower equilibria and the period one and two points bifurcated from them are marked. These are found using numerical continuation.

We now discuss the fundamental domains one by one.

Fundamental domain (1,1). In this domain there are only two stability regions. A stability diagram and phase portraits are displayed in Fig. 14. In the lower region ('SU') the upper equilibrium is unstable, while the

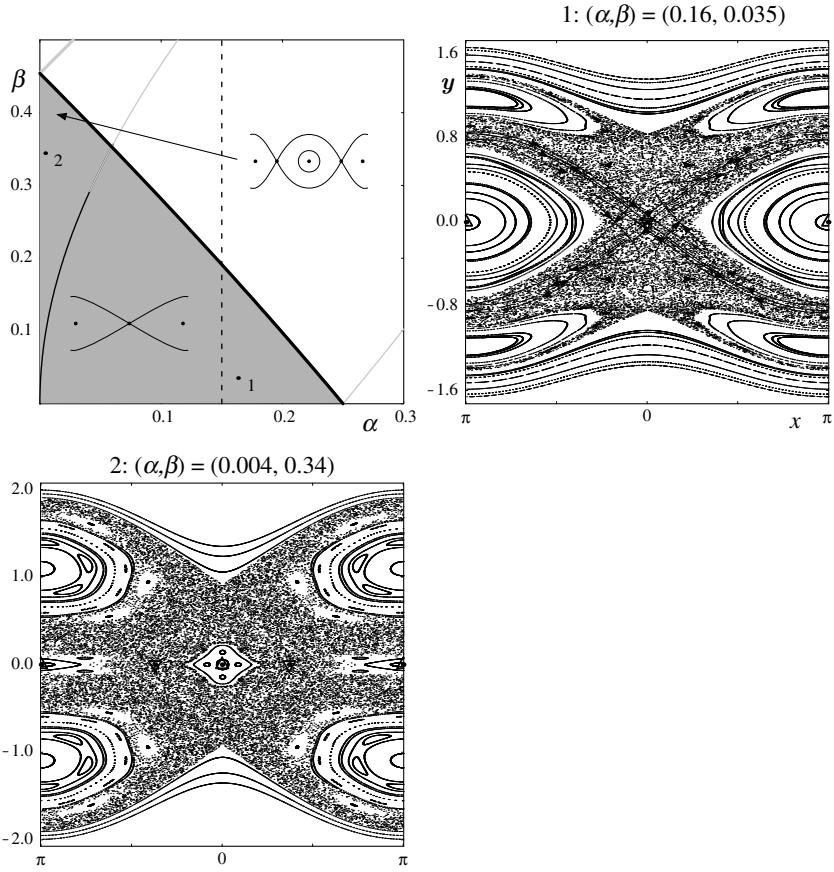

Figure 14. Stability diagram and phase portraits of the Poincaré map P in fundamental domain (1,1). The stability diagram also shows the bifurcation scheme. The stability curves in the fundamental domain under consideration are drawn in black, outside this domain they are grayed. The dashed vertical line in the stability diagram indicates the parameter line where a bifurcation diagram is made, see Section 4.4.1 for details. See Section 4.3 for more comments, and Fig. 3 for the coding of periodic points and invariant manifolds.

lower is stable, surrounded by invariant circles, see diagram 1 in Fig. 14. The chaotic sea can be associated to the unstable upper equilibrium, as explained in Section 4.

In the upper region ('SS') both equilibria are stable, see diagram 2, but with smaller stability domains than in diagram 1. The four satellites around the upper equilibrium have rotation number 1/4. They have been observed in another numerical study of the same system, see Acheson [2],

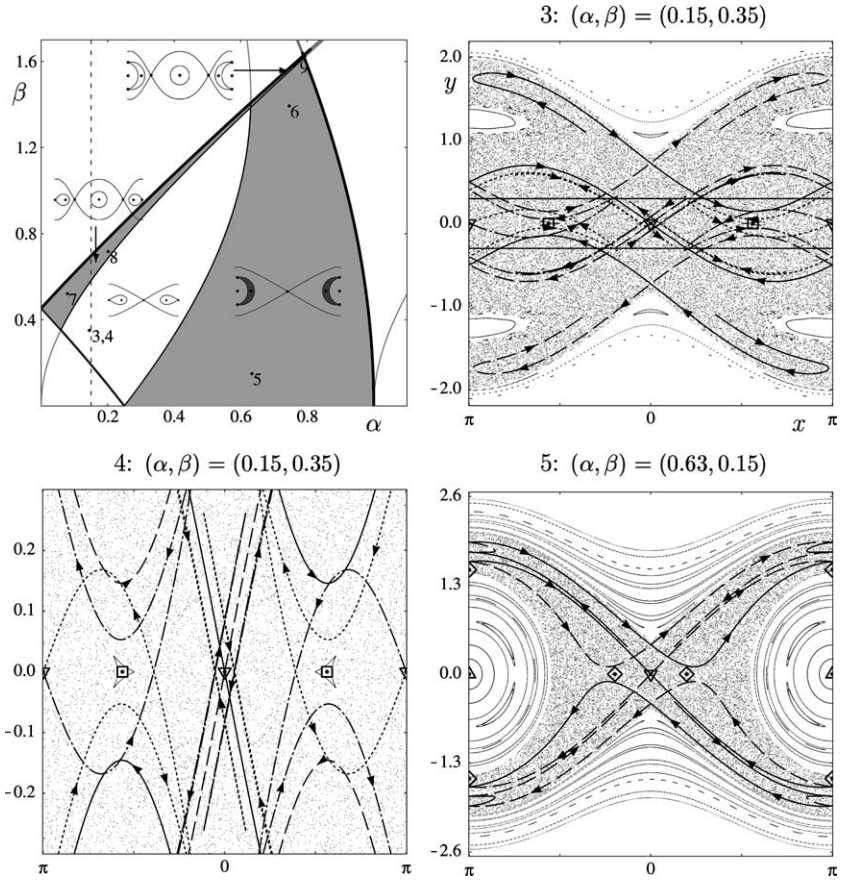

Figure 15. Stability diagram and phase portraits of P at parameter points in domain (2,1). Diagram 4 is a blowup of diagram 3, as indicated by the rectangle. To be continued in Fig. 16.

and are likely to come from a broken invariant circle. We note that both figures show two stable domains above and below the lower equilibrium, both around a stable fixed point. These are due to a broken invariant circle winding around the cylindrical phase space.

Fundamental domain (2,1). Figures 15 and 16 show a stability diagram and phase portraits. In the lower left region ('UU') the upper and lower equilibria are unstable. As suggested by the location of their invariant manifolds, see diagram 3 in Fig. 15, a large part of the chaotic sea can be associated to these two points. There is a stable period two orbit

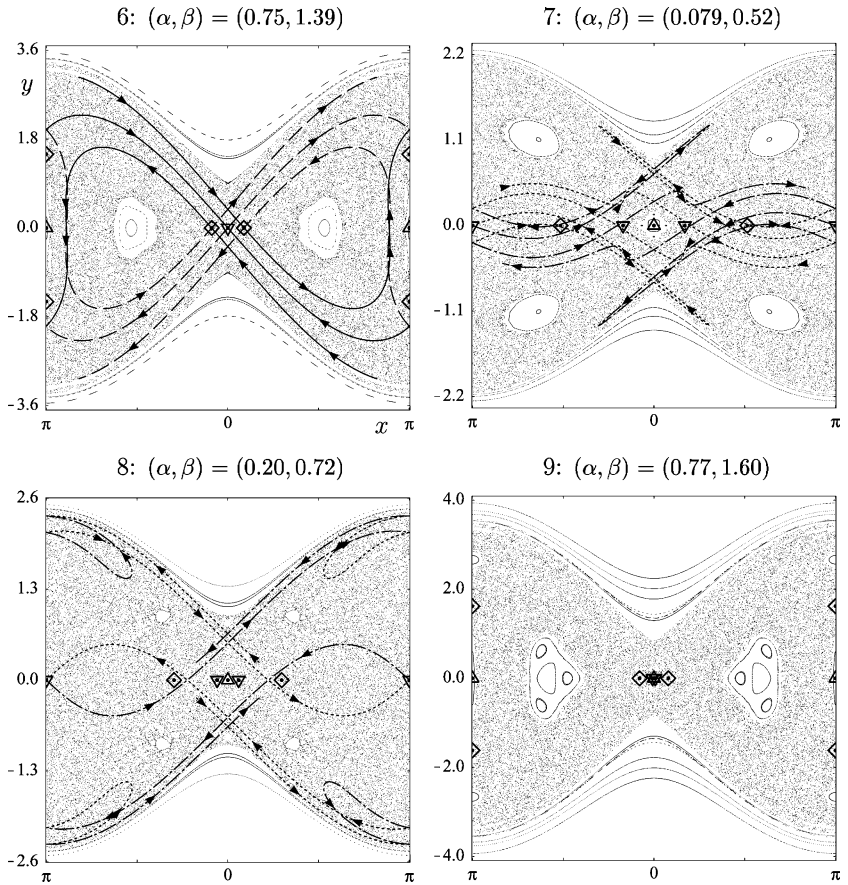

Figure 16. Continued from Fig. 15. Phase portraits of P at parameter points in domain (2,1).

on the x-axis, see diagram 3 and the blowup in diagram 4. This is the period two point that bifurcated from the lower equilibrium at the curve of period doubling bifurcations to the left of region 'UU'. Its stability domain decreases as β increases. Again there are two stable domains above and below the lower equilibrium.

In the lower right region ('SU') the lower equilibrium is stable, while the upper is unstable, causing a chaotic sea. For small β the Poincaré map is as in diagram 5. For larger β the stability domain of the lower equilibrium becomes smaller and smaller. Diagram 6 displays the situation near the upper edge of the region. The stable period two points already pres-

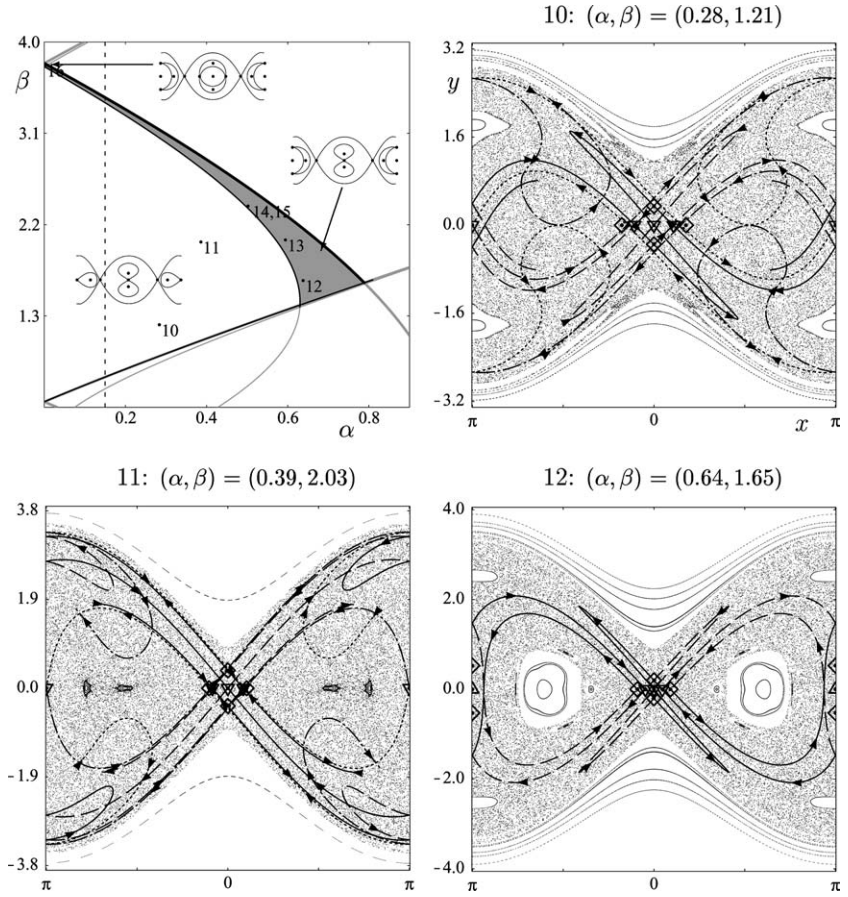

Figure 17. Stability diagram and phase portraits of P at parameter points in domain (2,2). To be continued in Fig. 18.

ent in diagram 3 have destabilized (in a pitchfork bifurcation, compare Fig. 20 below), and move towards the upper equilibrium as the parameters (α, β) increase. An unstable period two orbit has bifurcated from the lower equilibrium at the stability boundary between regions 'UU' and 'SU', and moves away from the equilibrium in y direction. At some parameter points a stable period two orbit, that did not bifurcate from one of the equilibria, is found on the x-axis, like in diagram 6.

In the upper left region ('US') the chaotic sea corresponds to the unstable lower equilibrium. Compared with diagram 3 there are two additional unstable fixed points on the x-axis that bifurcated from the

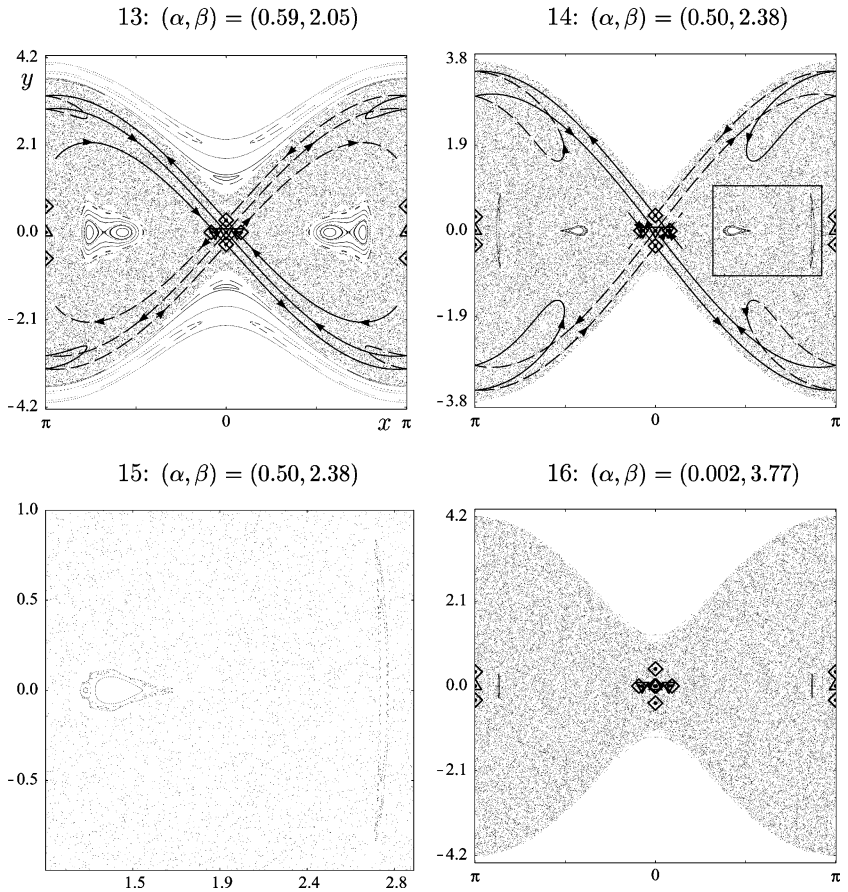

Figure 18. Continued from Fig. 17. Phase portraits of P at parameter points in domain (2,2). Diagram 15 is a blowup of diagram 14, as indicated. Diagram 16 is taken from region 'SS'.

upper equilibrium, that has become stable at this bifurcation. There are 4 satellites around the upper equilibrium, just as in diagram 2 of Fig. 14. The stable fixed points above and below the lower equilibrium of diagrams 1,2 and 3 have bifurcated, creating a stable period 2 orbit, that moves towards the upper equilibrium as α and β increase, see diagram 8 (also taken from region 'US').

In the upper right region ('SS') both stable equilibria have very small stability domains, see diagram 9. This region in the parameter plane is very narrow, and the Poincaré map does not vary much in it. Therefore

just one diagram is shown. The saddle fixed points bifurcated from the upper equilibrium at the stability boundary between regions 'SU' and 'SS' are very close to it and hardly distinguishable. Two unstable period two orbits, bifurcated from the lower equilibrium, can be found on the x-axis and on the line $x = \pi$. Like in region 'SU' there are two period two centers on the x, in this case surrounded by a period 6 satellite. The stable domains above and below the lower equilibrium are also present.

Fundamental domain (2,2). This domain consists of three regions. The stability diagram and Poincaré maps are displayed in Figs. 17 and 18. In the lower left region ('UU') the two unstable equilibria cause a large chaotic sea, see diagrams 10 and 11. Near the upper equilibrium there are two saddles on the x-axis and a period two orbit on the y-axis, all bifurcated from the upper equilibrium, and a period two orbit on the x-axis bifurcated from the lower equilibrium. Both period two orbits were stable when they bifurcated from the equilibria, but have destabilized in further bifurcations. At some parameter values we find four period two points on the x-axis, as in diagram 11. If we count the periodic points from left to right, then the first and third form an orbit, and so do the second and fourth.

In the lower right region ('SU') the lower equilibrium has stabilized, with a small stability domain. Two unstable period two points have bifurcated off in y direction. The chaotic sea can now be associated with the unstable upper equilibrium. Indeed, its manifolds seen to fill up a large part of the sea, see diagrams 12 to 14. In diagram 12 we find a stable period two orbit on the x-axis, surrounded by two (hardly visible) stable period four orbits. As β increases the period 2 points undergo a pitchfork bifurcation, resulting in two additional period 2 centers and saddles, compare diagram 13. As in diagram 11, the first and third center form one orbit, as do the second and fourth. Diagram 14 and its zoom in diagram 15 show that the centers and saddles move away from each other as β increases.

Region 'SS' is very small and the Poincaré map varies little in it. Both stable equilibria have very small stability domains. At some parameter points a stable period two orbit is found on the x-axis, as in diagram 16, where it lies close to the lower equilibrium. Apart from that there seems to be only chaos in the 'region of interest'.

4.3.2. The Fundamental Domain away from the Origin of the Parameter Plane

Figure 19 shows a stability diagram and phase portraits for the fundamental domain (12,6). The stability diagram does not show integrable skeletons, since these contain too many periodic points, but simply displays the fundamental domain under consideration, with an indication of

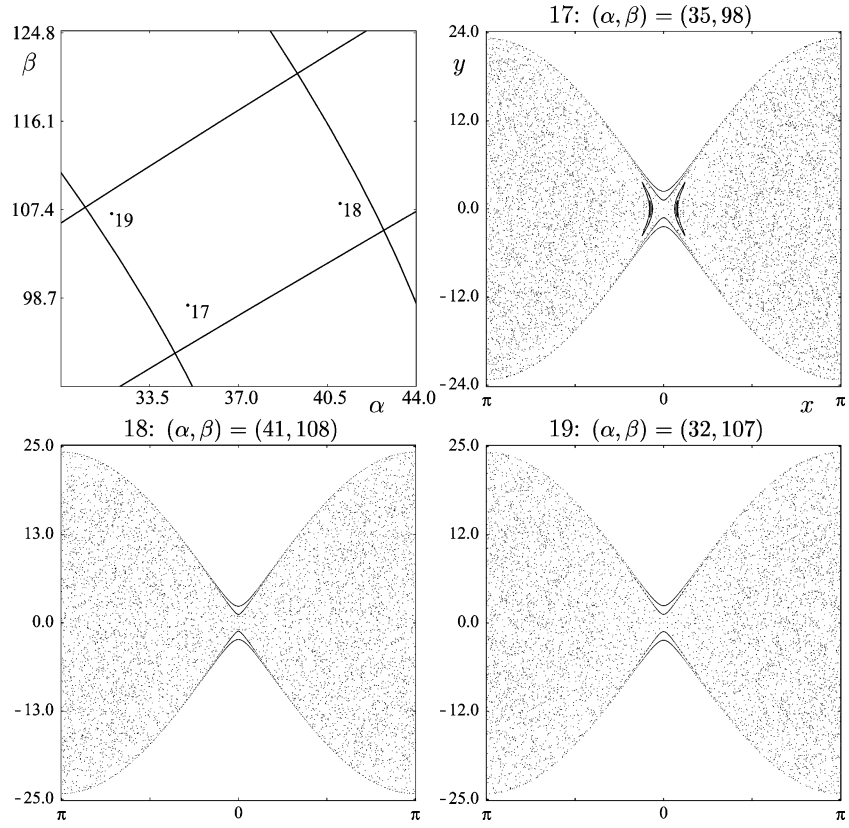

Figure 19. Stability diagram and phase portraits of the Poincaré map at parameter points in fundamental domain (12,6). See Section 4.3 for more comments on the dynamics.

the location of the computed phase portraits. The stable regions in the stability diagram are too narrow to be detected, therefore all phase portraits are taken from the region 'UU' where both equilibria are unstable.

The phase portraits display a representative collection of orbits of P. The periodic points that bifurcated from the upper and lower equilibrium are not shown, because there are so many. The phase portraits show only chaotic dynamics, except in diagram 17, where two stable regions surrounding a period two orbit are found on the x-axis. In other domains (of the same type) at large parameter values the dynamics is qualitatively the same.

4.4. Numerical Analysis

In this section some of the dynamical features encountered in the phase portraits of the Poincaré map are studied in more detail. The analysis is restricted to the domains near the origin of the parameter plane, since they show the most interesting dynamics. We first give an overview of the phenomena that we want to study, and then discuss them one by one.

The equilibria undergo bifurcations as determined by the skeleton. Section 4.4.1 presents numerically computed bifurcation diagrams of the equilibria that give more quantitative information, and show the stability types and bifurcations of the periodic points that bifurcated from the equilibria.

In some phase portraits, e.g. diagrams 6 and 9 in Fig. 16 or diagram 12 in Fig. 17, there is a stable period two orbit on the x-axis. It originates from a saddle-center bifurcation. This bifurcation, as well as a subsequent pitchfork bifurcation, resulting in a pair of period two orbits that can be observed in diagrams 11, 13, 14 and 15 in Figs. 17 and 18, is studied in Section 4.4.2.

The large stable regions above and below the lower equilibrium, see diagrams 1 and 2 in Fig. 14, diagram 3 in Fig. 15, diagram 9 in Fig. 16 and diagrams 10 and 12 in Fig. 17, are caused by a broken invariant circle. Section 4.4.3 presents a bifurcation analysis.

Finally, at resonances satellites are born around stable periodic points. For the equilibria and their satellites this is discussed in more detail in Section 4.4.4.

4.4.1. Bifurcation Diagrams of the Equilibria

To study the period one and two points of the Poincaré map P bifurcating from the upper and lower equilibria of the pendulum, we compute a bifurcation diagram at the lines $\alpha = 0.15$ in the parameter plane, with β as bifurcation parameter. It intersects the three domains near the origin of the parameter plane considered in Section 4.3, as indicated by vertical dashed line in the stability diagrams of Figs. 14–17. Other lines $\alpha =$ constant give rise to similar bifurcation diagrams.

Figure 20 displays the bifurcation diagrams. It shows branches of periodic points emanating from bifurcation points of the upper and lower equilibria, called *primary* branches and bifurcation points. The bifurcation points on the primary branches and the periodic points born there are called *secondary*. We note that for simplicity only the branches in one quadrant of (β, x, y)-space are displayed, the others are their symmetric counterpart with respect to the symmetries S and R, that is, under reflection in the (x, β) and (y, β) planes. Thus, at each primary bifurcation

point, and at some secondary bifurcation points, just one of the two newly born periodic points is shown. The diagrams are obtained by numerical continuation of periodic points. For general background and examples on numerical continuation we refer to Simó [73], Doedle *et al.* [31, 32], Kuznetsov [49] and Castellà and Jorba [29].

The bifurcation diagram of the upper equilibrium is qualitatively the same on all lines $\alpha = \text{constant}$, since on any such line one encounters the same bifurcation sequence as β increases from 0. This can be concluded from the stability diagram, see Figs. 1 and 4. For the lower equilibrium this is not true. For example, both stability curves originating from the first resonance point $(\alpha, \beta) = (\frac{1}{4}, 0)$ intersect the line $\alpha = \alpha_0$ for $\alpha_0 \in (0, \frac{1}{4})$, but none intersect this line for α_0 sufficiently large.

The bifurcations from the upper and lower equilibria found by Broer *et al.* [12, 13, 28], using perturbation theory, agree with the numerical results, compare Figs. 11 and 12. In all diagrams we see similar behavior: for the upper equilibrium, as β increases the primary branches first move away from the equilibrium along the x or y axis, but at higher β values they turn back. The secondary branches also go towards the upper equilibrium, but their location is not restricted to the axes.

As β increases, the primary branches of the lower equilibrium move either towards the upper equilibrium along the x-axis, or they escape in y direction along the line $x = \pi$, and do not seem to return. Some of the secondary branches return to the lower equilibrium, while others go to the upper equilibrium or go away in y direction. (Observe that the range of plotted y values is much larger for the lower equilibrium than for the upper equilibrium). Moreover it seems that no periodic point can be stable for a large interval of parameter values. Indeed, any stable periodic point rapidly bifurcates, while unstable points remain in existence over a large parameter range. This holds on primary as well as secondary branches.

4.4.2. The Saddle-center Bifurcation

In some of the phase portraits of Section 4.3 there are two or four stable period 2 orbits on the x-axis that did not bifurcate from one of the equilibria. We analyze these points by computing a bifurcation diagram and some phase portraits at relevant parameter values.

The bifurcation diagram is shown in Fig. 21. It has β as bifurcation parameter, while α is constant equal to 0.2836. (This line passes through the parameter point where the phase portrait of diagram 10 in Fig. 17 is taken).

The bifurcation diagram shows a period 2 saddle-center bifurcation, of the period 2 points to the left of the upper equilibrium. Those to the right are their images under P, and their bifurcation diagrams can be

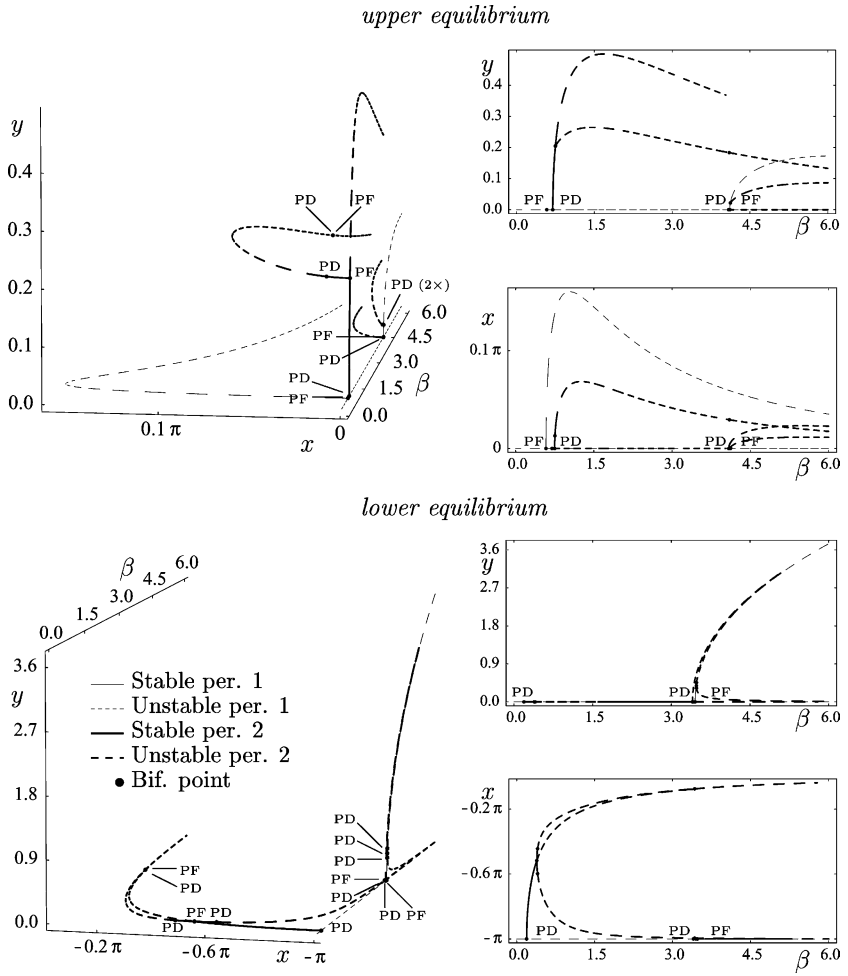

Figure 20. Bifurcation diagrams on the line $\alpha = 0.15$, and their projections onto the (β, x)- and (β, y)-planes, displaying primary and secondary branches of period one and two points of P. The straight lines parallel to the β-axis correspond to the positions of the equilibria. For simplicity only the branches in one quadrant of (β, x, y)-space are displayed, the others are their symmetric counterpart under reflection in the (β, x)- or (β, y)-plane. In the projections only the primary bifurcations are labelled.

obtained by a reflection $x \mapsto -x$. By symmetry, the branches coming from the saddle-center point satisfy $y = 0$. The stable orbit born at this bifurcation bifurcates further in a pitchfork bifurcation, creating the pair of sta-

ble period 2 orbits seen in for example in the phase portrait in Fig. 18, diagrams 13–15.

Phase portraits of the Poincaré map are shown in Fig. 22, for several parameter points on the line $\alpha = 0.2836$. Their captions state the parameter values, and the diagrams also display primary periodic points and invariant manifolds of (unstable) equilibria. In the first phase portrait, at $(\alpha, \beta) = (0.2836, 1.2134)$–this is the same as diagram 10 in Fig. 17–the saddle-center bifurcation has not yet occurred. The bifurcation takes place at $\beta \approx 1.4989$, corresponding to the second diagram. For higher β values there is one stable and one unstable period two orbit on the x-axis, see the diagram at $\beta = 1.6$. The stable orbit undergoes a pitchfork bifurcation at $\beta \approx 1.9423$, that creates a pair of stable period two orbits, see the last diagram. Here the first and third period two point (counted from the left) form an orbit, and so do the second and fourth.

In the last diagram two very small stable regions can be seen at $(x, y) = \approx (\pi, \pm 2.9)$. These are due to another saddle-center bifurcation. Its bifurcation diagram is given in Fig. 23. This bifurcation diagram is very similar to the previous one. In fact, the saddle-center bifurcation lies on a codimension one curve, that yields another curve of saddle-center bifurcations in the parameter plane, by the symmetry $T \circ U$, involving reflection in the β-axis, as a well as transformation in phase space. It can be shown that the second saddle-center bifurcation lies on the reflected curve, which explains the similarity. See Section 4.5 below for more details.

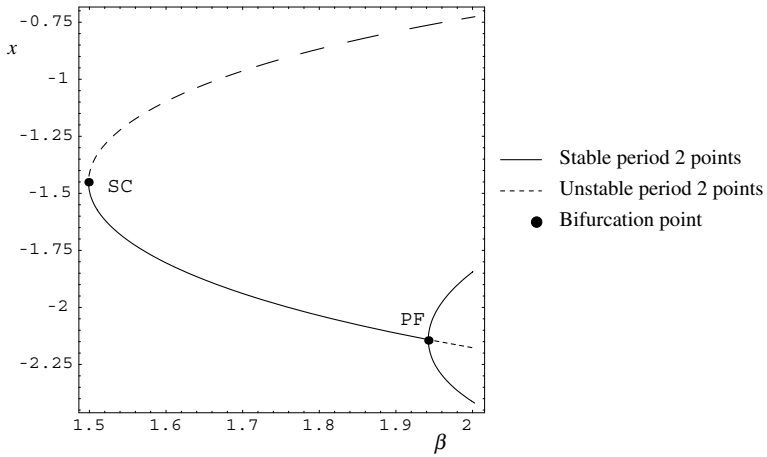

Figure 21. Bifurcation diagram on the line $\alpha = 0.2836$, displaying a saddle-center bifurcation. On the stable branch a pitchfork bifurcation occurs.

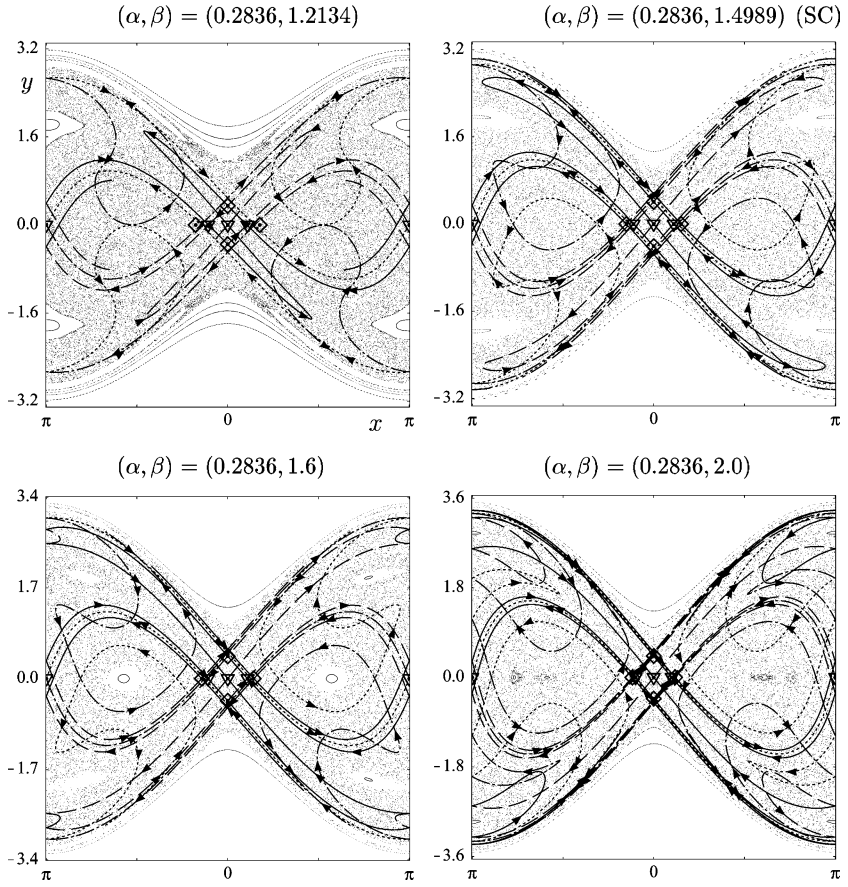

Figure 22. Phase portraits of the Poincaré map P at several parameter points on the line $\alpha = 0.2836$, solving a saddle-center and subsequent pitchfork bifurcation. All centers and saddles involved are of period 2, jumping from the right half plane to the left one, and back. See Section 4.4.2 for more comments.

The saddle-center bifurcation is possibly due to the Newhouse phenomenon, cf. [67, 69], which states that a homoclinic tangency, like the one in the top left diagram of Fig. 22, gives rise to infinitely many periodic points, created in saddle-center bifurcations at nearby parameter values. In Fig. 24 we illustrate this for period 8 points, that are created closer to the tangency than the period 2 points of Fig. 22. For fixed $\alpha = 0.2836$ as before, the two top diagrams of Fig. 24 show the x-axis and its image under P^8 shortly before and after a saddle center bifurcation, which takes place approximately at $\beta = 1.3505853379$. One of the period 8 stable points

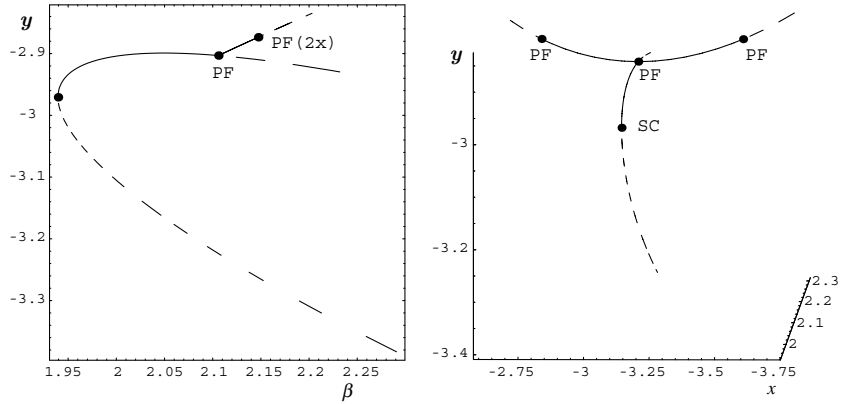

Figure 23. Bifurcation diagram on the line $\alpha = 0.2836$ of a second saddle-center bifurcation, taking place at a higher β value than the previous one, compare Fig. 21. Qualitatively the bifurcation diagram is the same. The branches of the saddle-center point lie in the plane $x = \pi$, but the other branches do not. Therefore a three-dimensional bifurcation diagram is added for clarity.

is shown in the bottom right diagram. At a slightly higher β value, namely $\beta \approx 1.3505853384$, this stable orbit is destroyed in a period doubling bifurcation, as shown in the bottom left diagram. In a similar way, if instead of period 8 we consider a period $2k > 8$, then patterns like the ones displayed in Fig. 24 appear. The value β_k at which the saddle-center bifurcation occurs tends to the value at which the homoclinic tangency is produced (roughly $\beta_{\text{hom}} = 1.2134$, as seen in Fig. 22 top left) when k tends to ∞.

4.4.3. The Broken Invariant Circle

The Poincaré map of the integrable system at $\beta = 0$ has a continuous family of invariant circles winding around the cylindrical phase space, and filling the region above the separatrix. (For simplicity we restrict to circles in the upper half cylinder $y > 0$.) For any $\beta > 0$, generically only circles satisfying a certain Diophantine condition persist. In particular, the resonant circle with rotation number 1 does not exist for *any* $\beta > 0$, and gives rise to the large stable domains above the lower equilibrium that can be seen in many phase portraits, for example diagrams 1 and 2 in Fig. 14.

Figure 25 displays a bifurcation diagram at the line $\alpha = 0.079$. For phase portraits we refer back to Fig. 2. The bifurcation diagram shows that the invariant circle under consideration is broken for all $\beta > 0$, yielding one stable and one unstable fixed point, at $x = \pi$ and $x = 0$, respectively. The saddle point does not bifurcate, while the center undergoes

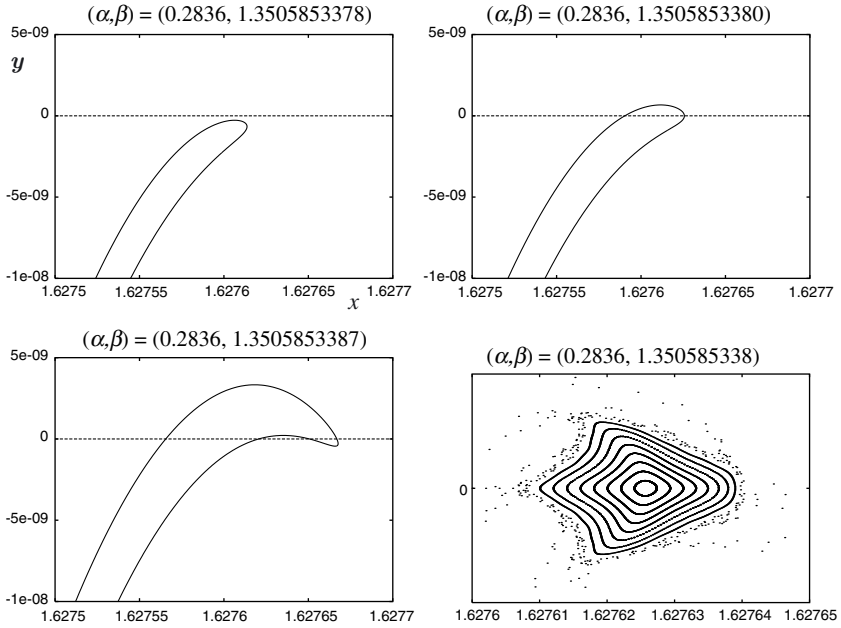

Figure 24. Illustration of the Newhouse phenomenon. Top, and bottom left: Part of the x-axis and its image under P^8, at the indicated parameter points, showing a saddle-center and subsequent period doubling bifurcation. Bottom right: one of the stable period 8 points that is created in the saddle-center bifurcation (and destroyed in the period doubling).

two period doubling bifurcations, followed by a pitchfork. The first period doubling bifurcation yields a stable period two orbit moving away from the line $x = \pi$, as illustrated by the third diagram of Fig. 2. This period two orbit in turn undergoes a pitchfork bifurcation, see the diagram at $\beta = 0.65$ in Fig. 2.

Furthermore, a subharmonic saddle-center bifurcation occurs at $\beta = 0.2148\ldots$, creating (for higher β values) a stable and an unstable period three orbit, near the stable fixed point coming from the broken invariant circle. The stable period three orbit can clearly be seen in the phase portrait at $\beta = 0.22$. It moves away from the stable fixed point as β increase. The unstable period three orbit intersects the stable fixed point at $\beta \approx 0.218$ and $(x, y) \approx (\pi, 1.14)$. At this point the eigenvalues of the linearized Poincaré map DP are (non-real) third roots of unity. This is a generic codimension one bifurcation sequence, compare Duistermaat [34]. A bifurcation diagram is presented in Fig. 26.

4.4.4. *Satellites*

This section deals with satellites of the equilibria, that is, strings of stable and unstable periodic orbits of period at least three, that encircle one of the equilibria. Orbits of period one and two are not discussed here: they are born at pitchfork and period doubling bifurcations, respectively, and are already dealt with above. For the forced pendulum satellites of period $q \geqslant 3$ are created in two different ways, where the symmetries and non-dissipativity of the system play an important role, compare [28].

The first is at a Poincaré-Birkhoff bifurcation, cf. [16,17,28], where a resonant invariant circle of P breaks. This bifurcation takes place at the α-axis, where the map is integrable and hence has resonant invariant circles. For $\beta \neq 0$ these generically break into satellites, with transversally intersecting stable and unstable manifolds of the saddle points, as follows from a subharmonic Melnikov theorem, see e.g. Guckenheimer and Holmes [37] and Broer and Takens [27]. On the α-axis the lower equilibrium is surrounded by a region of invariant circles, bounded by the separatrices. At a point $\alpha = \alpha_0$ on the α-axis the range of rotation numbers of these invariant circles is $(0, \sqrt{\alpha_0})$. Thus if β is increased from this point we only expect $p:q$ resonance bifurcations with $p/q < \alpha_0^2$.

The second is at a resonance of a fixed or a periodic point. As the eigenvalues of the linearized Poincaré map at this point pass through a

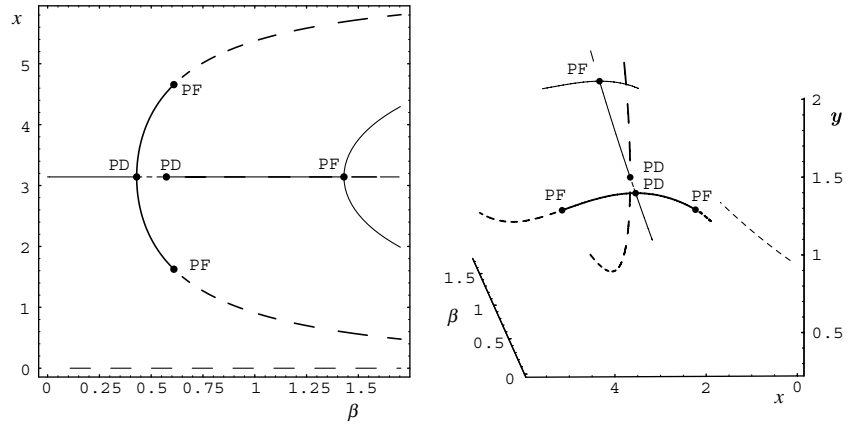

Figure 25. Bifurcation diagram on the line $\alpha = 0.079$, displaying the center and the saddle coming from the broken invariant circle with rotation number 1. The center undergoes two period doubling bifurcations and one pitchfork. Since some of the branches lie in the plane $x = \pi$, a three-dimensional bifurcation diagram is shown as well. Stability types and bifurcation points are indicated as before.

resonance, satellites are born there, see, e.g., Meyer [59], Takens [81] and Duistermaat [34], also compare Takens [80] and Arnol'd [5, 8] for the dissipative case. For the lower equilibrium the $p:q$ resonance bifurcation takes place at a curve in the parameter plane that passes through the point $\alpha = (p/q)^2$ on the α-axis. At a $p:q$ resonance curve the eigenvalues of the linearized Poincaré map pass through $e^{(\pm 2\pi i p/q)}$, but stay on the unit circle since P is area preserving. Thus the fixed point can only be unstable *at* the resonance.

Figure 27 shows resonance curves of order 3 and 6. Curves passing through the α-axis correspond to resonance of the lower, the others to resonances of the upper equilibrium. In fact, the resonance curves of the upper equilibrium are the images of those of the lower equilibrium under reflection in the β-axis (like the stability curves, cf. Section 2). Obviously the curves of resonance points have to lie in the stable regions of the parameter plane, and hence converge to the stability boundaries as β increases. An easy computation reveals that the resonance points of order 3 on the α-axis are given by

$$\alpha = \frac{1}{9}, \frac{4}{9}, \frac{16}{9}, \frac{25}{9}, \ldots,$$

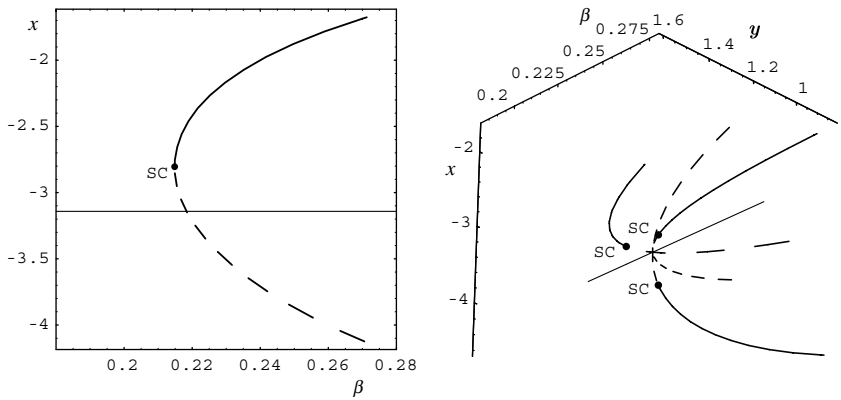

Figure 26. Right: bifurcation diagram on the line $\alpha = 0.079$ of a stable and an unstable period three orbit that are created in a saddle- center bifurcation point at $\beta = 0.2148\ldots$. On the left the projection to (β, x)-space of one of the three branches is shown. (The thicker curves now indicate period three points.) The unstable periodic points intersect the stable fixed point (from the broken invariant circle) at $\beta \approx 0.218$. The curves of periodic points passing through the saddle-center points lie in three different manifolds. Due to symmetry, one is the plane $x = \pi$.

and those of order 6 are given by

$$\alpha = \frac{1}{36}, \frac{25}{36}, \frac{49}{36}, \frac{121}{36}, \ldots,$$

as can be seen in the diagram.

In Fig. 28 we sketch (for the lower equilibrium) where the two bifurcations take place in the case of the 1:3 resonance, and also show the corresponding phase portraits. The latter only give a *qualitative* description of the dynamics involved, whereas the real map P of course has no heteroclinic connections, etc. Moreover, the width of the 'annulus' of $p:q$ resonant dynamics is $O(\sqrt{\beta})$ as $\beta \to 0$, hence resonant dynamics is a small phenomenon, cf. Duistermaat [34], Arnol'd [7] and Wiggins [82]. Finally, we observe that, due to the spatial and temporal symmetries S and R of P, at both resonance bifurcations two period 3 satellites are created simultaneously, leading to a total of 6 stable and 6 unstable periodic points.

Thus, if one starts for example at $(\alpha, \beta) = (1/4, 0)$, there is an invariant circle of rotation number 1/3 around the lower equilibrium. When β is increased, say to 1/10, this circle breaks into a string of islands. If we then go the left in the parameter plane until we hit the 1:3 resonance curve, the

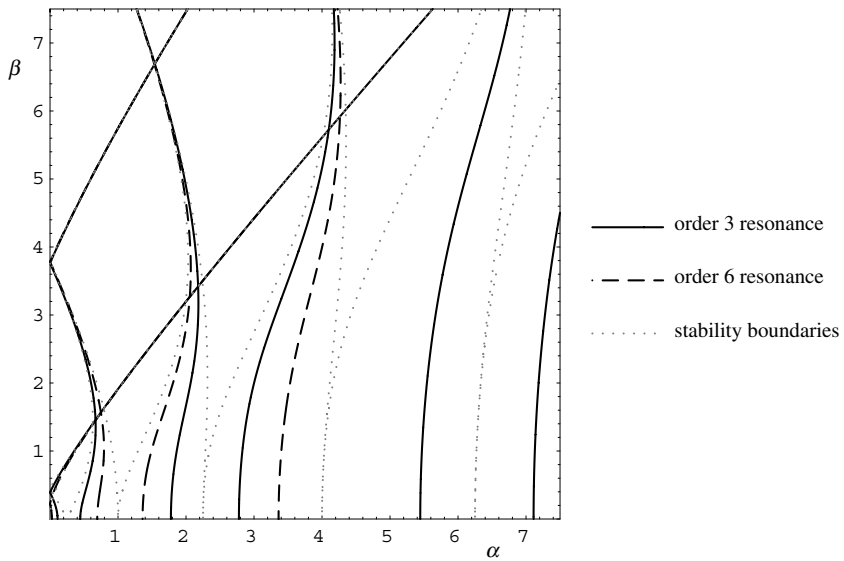

Figure 27. Diagram in the parameter plane showing curves of subharmonic bifurcation points, where period 3 or 6 points are created at the upper or lower equilibrium, as indicated. For clarity the stability boundaries of the equilibria are also indicated.

radius of the broken invariant circle shrinks to zero, and at the resonance curve it vanishes at the equilibrium.

Figure 29 displays a bifurcation diagram on the line $\alpha = 0.079 (< 1/9)$, showing four period 3 orbits, two stable and two unstable, branching off of the lower equilibrium in a 1:3 resonance bifurcation. The satellites are born in a third order resonance at the lower equilibrium, at $\beta \approx 0.195$. Poincaré maps before and after the bifurcation are shown in Fig. 2 (the first two diagrams). The diagram at $\beta = 0.22$ clearly shows two stable period three orbits around the lower equilibrium. We remark that in the preceding sections satellites of other periods were encountered in several phase portraits, e.g., period 4 satellites around the upper equilibrium in diagram 2 in Fig. 14 and diagram 7 in Fig. 16.

Remarks:

1. The $p : q$ subharmonic bifurcations of the forced pendulum take place in a Hamiltonian equivariant context with a discrete $\mathbb{Z}_2 \times \mathbb{Z}_2$ symmetry group, generated by the symmetries S and

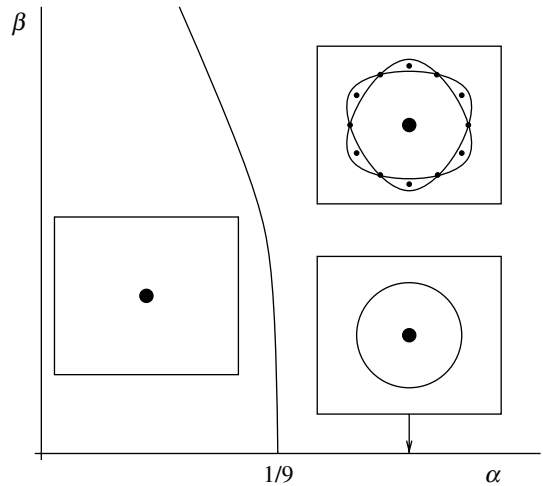

Figure 28. Sketch of the two types of 1:3 resonance bifurcations in the parameter plane, with phase portraits. For simplicity only the lower equilibrium and the 1:3 resonant dynamics are shown, for the regions to the left and right of the 1:3 resonance curve, and for the α-axis to the right of this curve. On the α-axis (for $\alpha > 1/9$) a Poincaré-Birkhoff bifurcation takes place, and on the 1:3 resonance curve passing through $\alpha = 1/9$ the lower equilibrium goes through a 1:3 resonance bifurcation. Observe that there are two stable and two unstable period 3 orbits, due to the symmetries S and R.

R. A complete analysis of the $p:q$ resonance in this setting requires an equivariant version of the subharmonic bifurcation theory developed by [34,59,81]. As far as we know no systematic study of these equivariant resonance bifurcations is available at this moment. However, for partial results in this direction, see [11,20,55].

2. In case the twist condition is violated at a stable fixed point, another bifurcation scenario is possible, leading to 'meandering' invariant circles. We do not discuss this matter here, but refer for more details to [33,75].

4.5. The Extended Stability Diagram

In the previous subsection we studied several bifurcations of saddle-center, pitchfork and period doubling type. They are all codimension one bifurcations, and hence take place on curves in the parameter plane. (For the bifurcations of the upper and lower equilibrium these are just the stability boundaries shown, e.g., in Fig. 4.) The curves are computed numerically using a continuation method, summarized in Fig. 30. It contains the following curves of bifurcation points:

– pitchfork and period doubling bifurcations of the equilibria, and secondary bifurcations of the same type on the primary branches

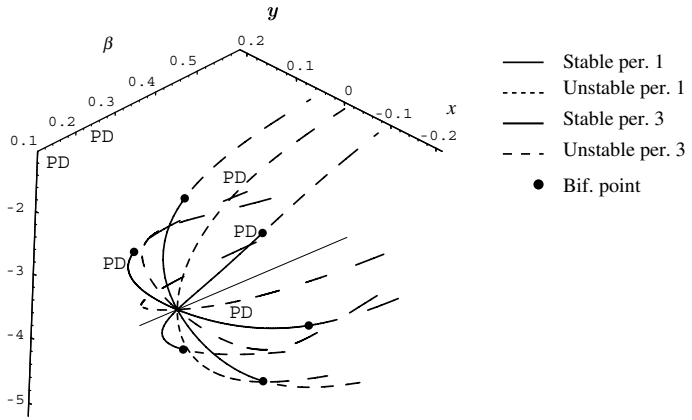

Figure 29. Bifurcation diagram on the line $\alpha = 0.079$ of the stable and unstable period three orbits (four in total) that are created in a bifurcation at the lower equilibrium point at $\beta \approx 0.195$. All orbits are created at the same bifurcation point due to symmetries. The stable periodic points undergo a period doubling bifurcation.

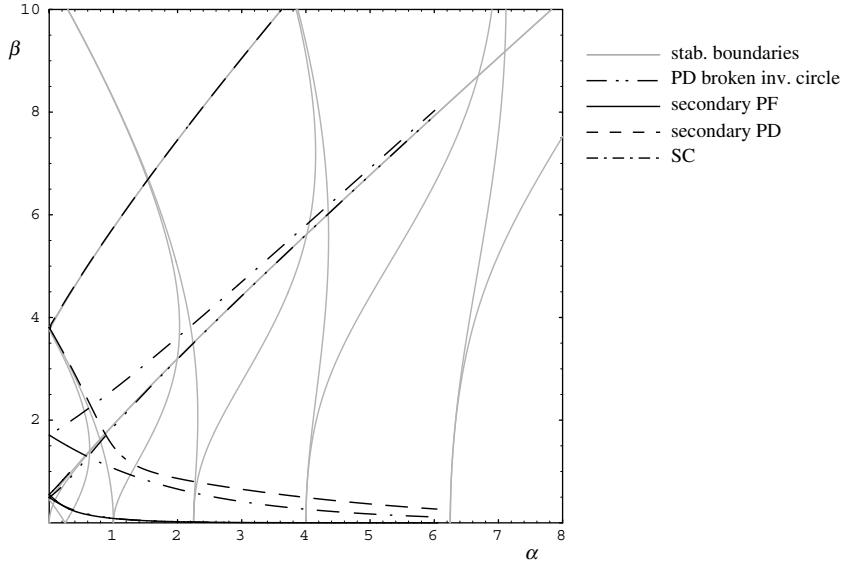

Figure 30. Curves of codimension one bifurcations in the parameter plane. The curves correspond to stability changes of the equilibria, a period doubling bifurcation of a broken invariant circle, bifurcations on the primary branches, and a saddle-center bifurcation, as indicated. See Section 4.5 for more comments.

of the equilibria. For the lower equilibrium, we consider two secondary bifurcations, namely the pitchfork on the primary branch coming from the leftmost stability boundary, and the period doubling on the branch born at the third boundary from the left, compare Fig. 20. The corresponding bifurcations are displayed for the upper equilibrium, namely the pitchfork and period doubling points on the second and fourth primary branches from below, respectively. See Section 4.4.1 for details on these bifurcations.

– saddle-center bifurcations corresponding to the large stable regions on the x-axis (and smaller ones above and below the lower equilibrium), discussed in Section 4.4.2.
– period doubling bifurcations of the stable fixed point coming from the broken invariant circle with rotation number 1 (i.e., the 1:1 torus of the corresponding vector field), cf. Section 4.4.3.

Curves of subharmonic bifurcations are shown in Fig. 27, and are omitted in the present diagram for clarity. Like the stability diagram, Fig. 30 is symmetric in both coordinate axes because of the symmetries T and U of P, and therefore only the first quadrant $\alpha, \beta \geqslant 0$ is displayed.

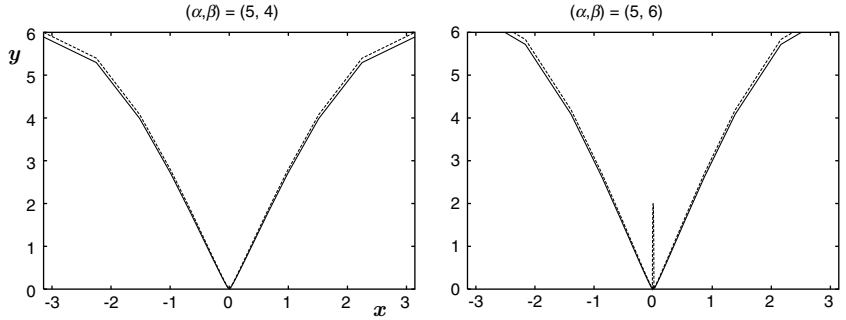

Figure 31. Comparison of a periodic orbit $(t, x(t), y(t))$ resulting from the broken 1:1 torus of the vector field (drawn line) with the frozen separatrix (dashed line), at $(\alpha, \beta) = (5, 4)$ (left diagram) and $(\alpha, \beta) = (5, 6)$ (right). The orbit is projected on the (x, y)- plane. The frozen separatrix is a two-dimensional manifold, introduced in Appendix A, and we plot the submanifold given by $x = x(t)$. The diagrams clearly illustrate that the orbit is close to the frozen separatrix, except near the upper equilibrium for $\beta > \alpha$.

As α increases, all curves seem to tend either to a stability boundary of the upper equilibrium, or to the α-axis.

The bifurcation curves seem to converge to the stability boundaries of the upper equilibrium as α and β go to infinity. It is remarkable that this is even true for bifurcations that are not related to this equilibrium (for example, the saddle-center bifurcations mentioned above). As far as we know, there is up to now no explanation for this. A possible approach, that we intend to take in future research, is to study the so-called separatrix map, cf. Simó and Treschev, that describes the dynamics in a neighborhood of the frozen separatrix of the pendulum system in a suitable rescaling, cf. section A. Some numerical evidence that the bifurcations we consider are described by this map is given in Fig. 31.

APPENDIX A. ADIABATIC ESTIMATES OF THE 'REGION OF INTEREST'

Adiabatic estimates for the size of the 'region of interest' are obtained in two regions in the parameter plane: for β small compared to α, and for large (α, β), 'near infinity', with $\alpha > \beta$. In these regions the adiabatic estimates are

$$y = 2\sqrt{\alpha},$$

to first approximation as $\beta \to 0$, and

$$y = 2\sqrt{\alpha + \beta},$$

to first approximation as $\alpha > \beta \to +\infty$, respectively. We first discuss the estimate for small β/α.

The stability diagram of figure 1 shows that the upper equilibrium is unstable if $\alpha > \beta \geqslant 0$, also see [65,71]. For $\alpha > 0$ and β small compared to α, the 'region of interest' is approximately bounded by the invariant manifolds of the unstable upper equilibrium of P. Indeed, for $\beta = 0$ the system is integrable, and the separatrices of the upper equilibrium exactly bound the 'region of interest', while outside this region only invariant circles exist. Thus by KAM theory the map P has invariant circles arbitrarily close to the invariant manifolds of the upper equilibrium, if $\beta > 0$ is sufficiently small. Neishtadt's theorem [66] implies that these manifolds lie in a neighborhood of the separatrices of the integrable system that vanishes as $\beta \to 0$. This proves the following lemma.

Lemma 4. *For $\alpha > 0$ the maximal y coordinate of the invariant manifolds of the unstable upper equilibrium satisfies*

$$y(\alpha, \beta) = 2\sqrt{\alpha} + f(\alpha, \beta),$$

where the remainder $f(\alpha, \beta)$ vanishes as $\beta \to 0$. The 'region of interest' is bounded by

$$y(\alpha, \beta) = 2\sqrt{\alpha},$$

to first approximation, as $\beta \to 0$.

To obtain an estimate for $\alpha, \beta \to +\infty$, with $\alpha > \beta$, we rescale to a slowly varying system by the following lemma:

Lemma 5 **(rescaling).** *Let $X = y\frac{\partial}{\partial x} + (\alpha + \beta\cos t)\sin x\frac{\partial}{\partial y} + \frac{\partial}{\partial t}$ be the vector field of the forced pendulum. Consider the rescaling*

$$(x, y, t : \alpha, \beta) \mapsto (\tilde{x}, \tilde{y}, \tilde{t}; \tilde{\alpha}, \tilde{\beta}, \varepsilon)(x, \varepsilon y, t, \varepsilon^2\alpha, \varepsilon^2\beta), X \mapsto \tilde{X} = \varepsilon X,$$

where $\varepsilon = (\alpha + \beta)^{-1/2}$. Then the rescaled vector field is Hamiltonian, $\mathcal{S}$-equivariant and $\mathcal{R}$-reversible, and is given by

$$X(x, y, t; \alpha, \beta, \varepsilon) = y\frac{\partial}{\partial x} + (\alpha + \beta\cos t)\sin x\frac{\partial}{\partial y} + \varepsilon\frac{\partial}{\partial t},$$

where the tildes are dropped for simplicity.

The proof is a straightforward computation, and is therefore omitted. The new parameters α, β satisfy $\alpha + \beta = 1$. The rescaled vector field X can be seen as a perturbation of the integrable, frozen vector field

$$X(x, y, t; \alpha, \beta, 0) = y\frac{\partial}{\partial x} + (\alpha + \beta\cos t)\sin x\frac{\partial}{\partial y}.$$

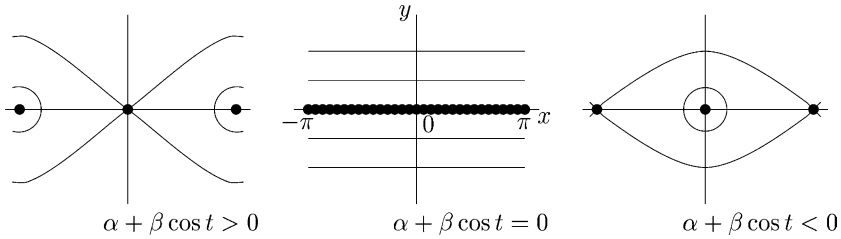

Figure 32. Sketch of the phase portrait of th e unperturbed, frozen system $X_{|\varepsilon=0}$. If $\alpha + \beta\cos t > 0$, then the upper equilibrium is unstable and the lower is stable. If $\alpha + \beta\cos t < 0$ (can only occur if $\beta > \alpha$), the stability types are reversed. If $\alpha + \beta\cos t = 0$ (only possible if $\beta \geqslant \alpha$), then the system is highly degenerate: all points on the x axis are in equilibrium.

In the original setting the frozen system is located at unbounded (y, α, β). The dynamics of the frozen system in the (x, y)- cylinder depends on the value of the 'parameter' t, see Fig. 32, while its integral curves coincide with the level sets of the Hamiltonian.

The region above the frozen separatrix is filled with invariant circles of the frozen system, and adiabatic theory can be applied to get an estimate on the 'lowest' invariant circle of the slowly varying system. Since $\alpha > \beta$, the unperturbed system has an unstable upper and a stable lower equilibrium, compare Fig. 32, and hence its lowest invariant circle is arbitrarily close to the separatrix

$$y = \sqrt{2(\alpha + \beta\cos t)(1 - \cos x)}.$$

By adiabatic theory, an orbit of the perturbed system remains $O(\varepsilon)$ close to the frozen orbit with the same initial condition for infinite time, if it does not intersect the frozen separatrix, see, e.g., [3, 5, 35, 68]. The 'lowest' frozen orbit that does not remain above the separatrix lies on the manifold

$$y = \sqrt{2(\alpha + \beta)(1 - \cos x)}.$$

Thus the maximal y-coordinate of the invariant manifolds of the upper equilibrium of the perturbed system is given by

$$y = 2\sqrt{\alpha + \beta} + \varepsilon\tilde{g}(\alpha, \beta, \varepsilon),$$

for some function $\tilde{g}$. Rescaling back to the original phase variables and parameters, and applying KAM theory, we arrive at the following lemma:

Lemma 6. *In the original coordinates, for $\alpha > \beta$ the maximal y coordinate of the invariant manifolds of the unstable upper equilibrium satisfies*

$$y(\alpha, \beta) = 2\sqrt{\alpha + \beta} + g(\alpha, \beta),$$

where $g(\alpha, \beta)$ is small compared to $\sqrt{\alpha+\beta}$ as $\alpha, \beta \to +\infty$. To first approximation as $\alpha, \beta \to +\infty$, the 'region of interest' is bounded by

$$y(\alpha, \beta) = 2\sqrt{\alpha+\beta}.$$

REFERENCES

1. Arnol'd, V. I., and Avez, A. (1968). *Ergodic Problems of Classical Mechanics, Mathematical Physics Monograph Series*, W.A., Benjamin.
2. Acheson, D. (1995). Multiple-nodding oscillations of a driven inverted pendulum. *Proc. Royal Soc. London A* **448**, 89–95.
3. Arnol'd, V. I. (1962). On the behavior of an adiabatic invariant under slow periodic variation of the Hamiltonian. *Soviet Math. Dokl.* **3**, 136–140.
4. Arnol'd, V. I. (1963). Proof of a theorem of A.N. Kolmogorov on the preservation of conditionally periodic motions under a small perturbation of the Hamiltonian (in Russian). *Russian Math. Surv.* **18**(5), 9–36.
5. Arnol'd, V. I. (1988). *Geometrical Methods in the Theory of Ordinary Differential Equations*, 2nd edn. Springer-Verlag.
6. Arnol'd, V. I. (1989). *Mathematical Methods of Classical Mechanics*, 2nd edn., volume 60 of *Graduate Texts in Mathematics*, Springer-Verlag.
7. Arnol'd, V. I. (1993). *Dynamical Systems. III*, Springer-Verlag. Mathematical aspects of classical and celestial mechanics, Translation of *Current Problems in Mathematics. Fundamental Directions, Vol. 3* (Russian), Akad. Nauk SSSR, Vessoyuz. Inst. Nauchn. i Tekhn. Inform., Moscow, 1985, Translation by A. Iacob.
8. Arnol'd, V. I. (1994). *Dynamical Systems. V*, Springer-Verlag, 1994. Bifurcation theory and catastrophe theory, Translation of *Current problems in mathematics. Fundamental directions*. Vol. 5 (*Russian*), Akad. Nauk SSSR, Vsesoyuz. Inst. Nauchn. i Tekhn. Inform., Moscow, 1986, Translation by N. D. Kazarinoff.
9. Benettin, G. (1988). Nekhoroshev-like results for Hamiltonian dynamical systems. In *Nonlinear Evolution and Chaotic Phenomena (Noto, 1987)*, Plenum, New York, pp. 121–146.
10. Back, A., Guckenheimer, J., Myers, M. R., Wicklin, F. J., and Worfolk, P. A. (1992). Dstool: Computer assisted exploration of dynamical systems. *Notices Am. Math. Soc.* **39**, 303–309.
11. Broer, H. W., Hoveijn, I., Lunter, G. A., and Vegter, G. (1998). Resonances in a spring-pendulum: algorithms for equivariant singularity theory. *Nonlinearity* **11**(16), 1569–1605.
12. Broer, H. W., Hoveijn, I., and van Noort, M. (1998). A reversible bifurcation analysis of the inverted pendulum. *Phys. D* **112**(1–2), 50–63. Time-reversal symmetry in dynamical systems (Warwick, 1996).
13. Broer, H. W., Hoveijn, I., van Noort, M., and Vegter, G. (1999). The inverted pendulum: a singularity theory approach. *J. Diff. Eq.* **157**, 120–149.
14. Broer, H. W., Huitema, G. B., and Sevryuk, M. B. (1996). *Quasi-Periodic Motions in Families of Dynamical Systems. Order Amidst Chaos*, vol. 1645 of *Lecture Notes in Mathematics*, Springer-Verlag.
15. Broer, H. W., Huitema, G. B., and Takens, F. (1990). Unfoldings of quasi-periodic tori. *Mem. Am. Math. Soc.* **83**(421), 1–81.
16. Birkhoff, G. D. (1913). Proof of Poincaré's geometric theorem. *Trans. Am. Math. Soc.* **14**(1), 14–22.
17. Birkhoff, G. D. (1925). An extension of Poincaré's last geometric theorem. *Acta Math.* **47**, 297–311.

18. Broer, H. W., and Levi, M. (1995). Geometrical aspects of stability theory for Hill's equations. *Arch. Rational Mech. Anal.* **131**(3), 225–240.
19. Broer, H. W., Levi, M., and Simó, C. In preparation.
20. Broer, H. W., Lunter, G. A., and Vegter, G. (1998). Equivariant singularity theory with distinguished parameters. Two case studies of resonant Hamiltonian systems. *Phys. D*, **112**(1–2), 64–80. Time-reversal symmetry in dynamical systems (Warwick, 1996).
21. Broer, H. W., van Noort, M., and Simó, C. In preparation.
22. Broer, H. W., and Roussarie, R. (2001). Exponential confinement of chaos in the bifurcation sets of real analytic diffeomorphisms. In Broer, H. W., Krauskopf, B., and Vegter, G. (eds.), *Global Analysis of Dynamical Systems-Festschrift Dedicated to Floris Takens for his 60th Birthday*, Inst. Phys. pp. 167–210.
23. Broer, H. W., Roussarie, R., and Simó, C. (1996). Invariant circles in the Bogdanov-Takens bifurcation for diffeomorphisms. *Ergodic Theo. Dynam. Syst.* **16**(6), 1147–1172.
24. Broer, H. W., and Simó, C. (1998). Hill's equation with quasi-periodic forcing: resonance tongues, instability pockets and global phenomena. *Bol. Soc. Brasil. Mat. (N.S.)*, **29**(2), 253–293.
25. Broer, H. W., and Simó, C. (2000). Resonance tongues in Hill's equation: a geometric approach. *J. Diff. Eq.* **166**(2), 290–327.
26. Broer, H. W., Simó, C., and Tatjer, J. C. (1998). Towards global models near homoclinic tangencies of dissipative diffeomorphisms. *Nonlinearity* **11**(3), 667–770.
27. Broer, H. W., and Takens, F. (1989). Formally symmetric normal forms and genericity. *Dyn. Report.* **2**, 39–59.
28. Broer, H. W., and Vegter, G. (1992). Bifurcational aspects of parametric resonance. *Dyn. Report. (N.S.)* **1**, 1–53.
29. Castellà, E., and Jorba, À, (2000). On the vertical families of two-dimensional tori near the triangular points of the bicircular problem. *Celestial Mech. Dyn. Astronom.* **76**(1), 35–54.
30. Chierchia, L., and Zehnder, E. (1989). Asymptotic expansions of quasiperiodic solutions. *Ann. Scuola Norm. Sup. Pisa Cl. Sci. (4)* **16**(2), 245–258.
31. Doedel, E., Keller, H. B., and Kernévez, J. -P. (1991). Numerical analysis and control of bifurcation problems. I. Bifurcation in finite dimensions. *Int. J. Bifur. Chaos Appl. Sci. Engrg.* **1**(3), 493–520.
32. Doedel, E., Keller, H. B., and Kernévez, J. -P. (1991). Numerical analysis and control of bifurcation problems. II. Bifurcation in infinite dimensions. *Int. J. Bifur. Chaos Appl. Sci. Engrg.* **1**(4), 745–772.
33. Dullin, H. R., Meiss, J. D., and Sterling, D. (2000). Generic twistless bifurcations. *Nonlinearity* **13**(1), 203–224.
34. Duistermaat, J. J. (1984). Bifurcation of periodic solutions near equilibrium points of Hamiltonian systems. In *Bifurcations Theory and Applications (Montecatini, 1983)*, Vol. 1057 of *Lecture Notes in Mathematics*, Springer Verlag, pp. 57–105.
35. Elskens, Y., and Escande, D. F. (1991). Slowly pulsating separatrices sweep homoclinic tangles where islands must be small: an extension of classical adiabatic theory. *Nonlinearity* **4**(3), 615–667.
36. Fassò, F. (1990). Lie series method for vector fields and Hamiltonian perturbation theory. *Z. Angew. Math. Phys.* **41**(6), 843–864.
37. Guckenheimer, J., and Holmes, P. (1983). *Nonlinear Oscillations, Dynamical Systems, and Bifurcations of Vector Fields*, Vol. 42 of Applied Mathematical Sciences, Springer-Verlag.
38. Giorgilli, A., Lazutkin, V. F., and Simó, C. (1998). Visualization of a hyperbolic structure in area preserving maps. *Reg. Chaotic Dyn.* **2**(3–4), 47–61. Correction in same journal, **3**(2), 115.

39. Hale, J. K. (1992). *Oscillations in Nonlinear Systems*, McGraw-Hill, Re-publication: Dover publications.
40. Hale, J. K. (1980). *Ordinary Differential Equations*, 2nd edn. Wiley-Interscience, Krieger.
41. Hénon, M., and Heiles, C. (1964). The applicability of the third integral of motion; some numerical experiments. *Astronom. J.* **69**, 73–79.
42. Huitema, G. B. (1988). Unfoldings of Quaisperiodic Tori. PhD thesis, University of Groningen.
43. Jorba, À., and Villanueva, J. (1997). On the normal behaviour of partially elliptic lower-dimensional tori of Hamiltonian systems. *Nonlinearity* **10**(4), 783–822.
44. Jorba, À., and Zou, M. On the numerical integration of ode by means of high-order taylor methods. preprint.
45. Kim, S. -Y., and Hu, B. (1998). Resurrection of an inverted pendulum. *Chatoic Dynamics*, Electronic journal: http://xxx.lanl.gov/abs/chaodyn/9802015vl.
46. Krauskopf, B., and Osinga, H. M. (2000). Investigating torus bifurcations in the forced van der Pol oscillator. In *Numerical Methods for Bifurcation Problems and Large-scale Dynamical Systems (Minneapolis, MN, 1997)*, Vol. 119 of *IMA Vol. Math. Appl.* Springer-Verlag, New York, pp. 199–208.
47. Kolmogorov, A. N. (1954). On conservation of conditionally periodic motions for a small change in Hamilton's function (in Russian). *Dokl. Akad. Nauk SSSR (N.S)*, **98** 527–530. English translation in Lecture Notes in Physics **93**, 51–56.
48. Kolmogorov, A. N. (1957). Théorie générale des systèmes dynamiques et mécanique classique. In *Proceedings of the International Congress of Mathematicians, Amsterdam, 1954*, Vol. 1, Erven, P. Noordhoff N. V., Groningen; North-Holland Publishing Co., Amsterdam, English translation in [**?**].
49. Kuznetsov, (1995). *Elements of Applied Bifurcation Theory*, Vol. 112 of *Applied Mathematical Sciences*, Springer-Verlag.
50. Levi, M. (1988). Stability of the inverted pendulum – a topological explanation. *SIAM Rev.* **30**(4), 639–644.
51. Levi, M. (1900). KAM theory for particles in periodic potentials. *Ergod. Th. Dyn. Sys.* **10** 777–785.
52. Levi, M. (1991). Quasiperiodic motions in superquadratic time-periodic potentials. *Comm. Math. Phys.* **143**(1), 43–83.
53. Laederich, S., and Levi, M. (1991). Invariant curves and time-dependent potentials. *Ergod. Th. Dyn. Sys.* **11**,(2) 365–378.
54. Lichtenberg, A. J., and Lieberman, M. A. (1992). *Regular and Chatoic Dynamics*, Vol. 38 of *Applied Mathematical Sciences*, 2nd edn., Springer-Verlag.
55. Lunter, G. (1999). *Bifurcations in Hamiltonian systems: computing singularities by Gröbner bases.* PhD thesis, Rijksuniversiteit Groningen.
56. Levi, M., and Weckesser, W. (1995). Stabilization of the inverted linearized pendulum by high frequency vibrations. *SIAM Rev.* **37**(2), 219–223.
57. Mathieu, É. (1868). Mémoire sur le mouvement vibratoire d'une membrane de forme elliptique. *J. Math. Pures Appl.* **13**, 137–203.
58. McLaughlin, J. B. (1981). Period-doubling bifurcations and chaotic motion for a parametrically forced pendulum. *J. Stat. Phys.* **24**(2), 375–388.
59. Meyer, K. R. (1970). Generic bifurcation of periodic points. *Trans. Am. Math. Soc.* **149**, 95–107.
60. Moser, J. (1962). On invariant curves of area-preserving mappings of an annulus. *Nachr. Akad. Wiss. Göttingen. Math-Phys. Kl.* **II**, 1–20.
61. Moser, J. (1967). Convergent series expansions for quasi- periodic motions. *Math. Ann.* **169**, 136–176.

62. Moser, J. (1968). Lectures on Hamiltonian systems. *Mem. Am. Math. Soc.* **81**, 1–60.
63. Moser, J. (1989). Minimal foliations on a torus. In Giaquinta, M. (ed.), *Topics in Calculus of Variations (Montecatini Terme, 1987)*, Vol. 1365 of *Lecture Notes in Mathematics*, Springer-Verlag, pp. 62–99.
64. Moser, J. (1989). Quasi-periodic solutions of nonlinear elliptic partial differential equations. *Bol. Soc. Brasil. Mat. (N.S.)* **20**(1), 29–45.
65. Meixner, J., and Schäfke, F. W. (1954). *Mathieusche Funktionen und Sphäroidfunktionen*, Springer-Verlag.
66. Neishtadt, A. I. (1984). The separation of motions in systems with rapidly rotating phase. *J. Appl. Math. Mech.* **48**(2), 133–139.
67. Newhouse, S. E. (1974). Diffeomorphisms with infinitely many sinks. *Topology* **13**, 9–18.
68. Neishtadt, A. I., Sidorenko, V. V., and Treschev, D. V. (1997). Stable periodic motions in the problem on passage through a separatrix. *Chaos* **7**(1), 2–11.
69. Olvera, A., and Simó, C. (1993) Elliptic non-Birkhoff periodic orbits in the twist maps. *Int. J. Bifur. Chaos Appl. Sci. Engrg.* **3**(1), 165–185.
70. Pöschel. J., (1982). Integrability of Hamiltonian systems on Cantor sets. *Comm. Pure Appl. Math.* **35**(5), 653–696.
71. van der Po, B., and Strutt, M. J. O. (1928). On the stability of the solutions of Mathieu's equation. *London Edinburgh Dublin Philos. Mag.* **5**, 18–38.
72. Robinson, R. C. (1970). Generic properties of conservative systems I, II. *Am. J. Math.* **92**, 562–603 and 897–906.
73. Simó, C. (1989). On the analytical and numerical approximation of invariant manifolds. In Benest, D., and Froeschlé, C. (eds.), *Les méthodes modernes de la mécanique céleste*, Goutelas, pp. 285–329.
74. Simó, C. (1994). Averaging under fast quasiperiodic forcing. In *Hamiltonian mechanics (Toruń, 1993)*, Plenum, New York, pp. 13–34.
75. Simó, C. (1998). Invariant curves of analytic perturbed nontwist area preserving maps. *Regul. Chaotic Dyn.* **3**(3), 180–195.
76. Simó, C. (2001). Global dynamics and fast indicators. In Broer, H. W., Krauskopf, B., and Vegter G. (eds.), *Global Analysis of Dynamical Systems-Festschrift Dedicated to Floris Takens for his 60 the Birthday*, Institute of Physics Publishing. pp. 373–389.
77. Simó, C., and Treschev, D. V. Evolution of the "last" invariant curve in a family of area preserving maps. preprint.
78. Simó, C., and Treschev, D. V. Stability islands in the vicinity of separatrices of near-integrable symplectic maps. preprint.
79. Stoker, J. J. (1950). *Nonlinear Vibrations in Mechanical and Electrical Systems*, Interscience Publishers, New York.
80. Takens, F. (2001). Forced oscillations and bifurcations. In *Applications of global analysis I (Sympos., Utrecht State Univ., Utrecht, 1973)*, number 3 in Comm. Math. Inst. Rijksuniv. Utrecht, Math. Inst. Rijksuniv. Utrecht, Utrecht, 1–59, 1974 reproduced in *Global analysis of dynamical systems – Festschrift dedicated to Floris Takens for his 60th birthday*, Institute of Physics Publishing, pp. 1–61.
81. Takens, F. (1974). *Introduction to Global Analysis*, Mathematisch Instituut, Rijksuniversiteit Utrecht, Utrecht. Lectures held at Utrecht State University, October–December, 1972, Communications of the Mathematical Institute, Rijksuniversiteit Utrecht, No. 1973-2.
82. Wiggins, S. (1990). *Introduction to Applied Nonlinear Dynamical Systems and Chaos*, Vol. 2 of *Texts in Applied Mathematics*, Springer-Verlag.
83. Weinstein, M. I., and Keller, J. B. (1988). Hill's equation with a large potential. *SIAM J. Appl. Math.* **45**(2), 200–214.

84. Weinstein, M. I., and Keller, J. B. (1987). Asymptotic behaviour of stability regions for Hill's equation. *SIAM J. Appl. Math.* **47**(5), 941–958.
85. You, J. (1990). Invariant tori and Lagrange stability of pendulum-type equations. *J. Diff. Eq.* **85**, 54–65.